



Topology optimization of MEMS resonators with target eigenfrequencies and modes

Giannini, Daniele; Aage, Niels; Braghin, Francesco

Published in:
European Journal of Mechanics, A/Solids

Link to article, DOI:
[10.1016/j.euromechsol.2021.104352](https://doi.org/10.1016/j.euromechsol.2021.104352)

Publication date:
2022

Document Version
Peer reviewed version

[Link back to DTU Orbit](#)

Citation (APA):
Giannini, D., Aage, N., & Braghin, F. (2022). Topology optimization of MEMS resonators with target eigenfrequencies and modes. *European Journal of Mechanics, A/Solids*, 91, Article 104352. <https://doi.org/10.1016/j.euromechsol.2021.104352>

General rights

Copyright and moral rights for the publications made accessible in the public portal are retained by the authors and/or other copyright owners and it is a condition of accessing publications that users recognise and abide by the legal requirements associated with these rights.

- Users may download and print one copy of any publication from the public portal for the purpose of private study or research.
- You may not further distribute the material or use it for any profit-making activity or commercial gain
- You may freely distribute the URL identifying the publication in the public portal

If you believe that this document breaches copyright please contact us providing details, and we will remove access to the work immediately and investigate your claim.

Highlights

Topology optimization of MEMS resonators with target eigenfrequencies and modes

Daniele Giannini, Niels Aage, Francesco Braghin

- An efficient topology optimization approach for MEMS resonators is proposed
- Focus is given to industrially relevant layouts with suspended proof masses
- The first structural eigenmodes are controlled considering different target eigenfrequencies
- Numerical efficiency is obtained through the use of reduced order models
- The method is demonstrated for single mass and tuning fork MEMS gyroscopes

Topology optimization of MEMS resonators with target eigenfrequencies and modes

Daniele Giannini^{a,b,*}, Niels Aage^c and Francesco Braghin^a

^aDepartment of Mechanical Engineering, Politecnico di Milano, Via G. La Masa 1, 20156 Milano (MI), Italy

^bDepartment of Civil Engineering - Structural Mechanics Section, KU Leuven, Kasteelpark Arenberg 40, 3001 Leuven, Belgium

^cCentre for Acoustic-Mechanical Micro Systems, Department of Mechanical Engineering, Technical University of Denmark, Nils Koppels Alle, Building 404, DK-2800 Kgs. Lyngby, Denmark

ARTICLE INFO

Keywords:

Topology optimization
MEMS resonators
Target eigenfrequencies
Reduced order models
Minimum length scale
Method of moving asymptotes

ABSTRACT

In this paper we present a density based topology optimization approach to the synthesis of industrially relevant MEMS resonators. The methodology addresses general resonators employing suspended proof masses or plates, where the first structural vibration modes are typically of interest and have to match specific target eigenfrequencies. As a significant practical example we consider MEMS gyroscope applications, where target drive and sense eigenfrequencies are prescribed, as well as an adequate distance of spurious modes from the operational frequency range. The 3D dynamics of the structure are analyzed through Mindlin shell finite elements and a numerically efficient design procedure is obtained through the use of model order reduction techniques based on the combination of multi-point constraints, static approximations and static reduction. Manufacturability of the optimized designs is ensured by imposing a minimum length scale to the geometric features defining the layout. Using deterministic, gradient-based mathematical programming, the method is applied to the design of both single mass and tuning fork MEMS resonators. It is demonstrated that the proposed methodology is capable of meeting the target frequencies and corresponding modes fulfilling common industrial requirements.


1. Introduction

Micro Electro Mechanical Systems (MEMS) are one of the most disruptive technologies of the 21st century. To a large extent, they form the basis for the forthcoming Internet-of-Things (IoT) revolution, that will increase the interaction between electronic devices and between devices and real world, facilitating smart living for humans and machine-to-machine communication (M2M). In this framework, MEMS are used as ultra-compact and high performance sensors and actuators in different domains, including consumer electronics, automotive safety, autonomous driving, avionics, smart transportation systems, energy grids, and healthcare facilities.

MEMS resonators are small electromechanical structures that vibrate at high frequencies. They are key components that are extensively employed in many of the aforementioned applications, such as frequency selection (e.g. MEMS radio-frequency (RF) and intermediate-frequency (IF) filters [1, 2, 3]), timing (i.e. MEMS oscillators [4, 5, 6]), inertial detection (i.e. MEMS accelerometers and gyroscopes, [7, 8, 9]), optical signals manipulation (e.g. scanning micromirrors [10, 11]), energy harvesting [12, 13], and mass/chemical sensing purposes [14, 15, 16]. MEMS resonators are manufactured as extruded planar geometries with a given thickness, usually relying on silicon etching processes [17]: the structure has therefore an essentially 2D layout, but in general it exhibits relevant 3D dynamics. In typical applications, the micromechanical structure is forced into vibrations by converting an input electrical signal into a force which is used to excite the device. Vibrations of the structure are then picked up and often converted back into an electrical signal through various capacitive, piezoelectric, thermal or piezoresistive transduction techniques.

The mechanical characteristics of MEMS resonators, and MEMS devices in general, are typically designed merging predefined simple elements, typically masses and flexural or torsional springs made by simple or folded beams. The traditional design procedure is trial and error, and the design engineer has to iterate the manual tuning of the position and dimensions of the mechanical elements in order to satisfy the device requirements given by the application. This results in a much time-consuming and expensive design process, that also depends on the design engineer experience [18, 19]. As recent market developments push towards continuous miniaturisation of MEMS devices and reduction

*Corresponding author

 daniele.giannini@polimi.it (D. Giannini)

ORCID(s): 0000-0002-1214-2570 (D. Giannini); 0000-0002-3042-0036 (N. Aage); 0000-0002-0476-4118 (F. Braghin)

of power consumption, the design procedure of the devices becomes more and more crucial, and the development of automatic design tools based on structural optimization becomes fundamental to ensure industrial progress [18]. Structural optimization methods can, crudely, be put into two different categories, depending on the level of design freedom they provide.

The simplest, and most restrictive structural optimization approaches, are size and/or shape optimization: in this case, the dimensions, position and shapes of the mechanical elements constituting the MEMS device are parametrized by a set of design variables. Numerical optimization is then employed to obtain the desired performance, usually relying on FEM simulations. The application of size/shape optimization to the design of MEMS resonators covers a wide extent of purposes, such as extending the operational frequency range of piezoelectric MEMS energy harvesters [20], tailoring mechanical nonlinearities through non-uniform beam profiles [21], or improving temperature stability of tuning fork resonators through slots in the resonator beams [22]. Another interesting application is the design of MEMS gyroscopes, that are microsensors able to measure the external angular rate, and are based on the interaction of different natural modes due to Coriolis effects. Early works are focused on the tuning of the structural natural frequencies related to specific mode shapes [23, 24], while an automatic design environment for MEMS resonators is presented in [25]: it allows the parametric generation of the structure geometry, the simulation of its behaviour via 3D FEM, and the layout optimization by means of gradient based techniques, focusing both on target natural frequencies and mode shapes, and on the maximization of the sensor response to the external angular rate. However, both size and shape optimization does not allow for new features, such as additional springs or new holes, to appear, i.e. the initial conceptual configuration remains unchanged.

Another approach to structural optimization is topology optimization: this method does not require any initial parameterization of the layout by the design engineer, but directly looks for the best way to distribute the material within the available design space. This makes the design procedure much more free to explore different structural shapes and able to go beyond usual design concepts, fostering innovation. Since its introduction for stiffness maximization subject to a constraint on the available material [26], the method has evolved to be able to treat problems related to dynamics and vibrations, such as frequency optimization [27, 28, 29, 30], also in cellular structures [31, 32], dynamic compliance optimization [33, 34] and frequency constraints [35]. The application of topology optimization to MEMS resonators ranges from the control of the first eigenfrequencies [36], to thermo-elastic damping reduction [37], to electric power maximization in energy harvesters [38]. Also, in [39] optimal auxetic structures are designed to properly propagate the motion in the resonator from actuated to non actuated masses, while in [40] the reliability of capacitive RF MEMS switches is improved by reducing the impact of intrinsic biaxial stresses and stress gradients on the switch's membrane.

In a recent publication, the authors presented a topology optimization methodology for MEMS resonators, tailored for the design of MEMS gyroscopes [41]. The focus was on method development and the design task was confined to the suspending structure of single mass resonators limited to in-plane 2D dynamics. The paper proposed three different optimization formulations with varying numerical complexity, which were evaluated on an academic benchmark example and then translated to a more realistic design case.

The focus of the present paper is to extend the topology optimization approach developed in [41] to the design of industrially relevant MEMS resonators. More general planar structures employing suspended proof masses or plates are therefore here addressed, and their complete 3D dynamics are considered. The method is applied to control the first eigenfrequencies of both single mass and double mass tuning fork MEMS resonators for gyroscope applications, when imposing different target eigenfrequencies in an industrially acceptable range. In particular, we employ a discretization by Mindlin shell finite elements in the analysis, and we propose the use of reduced order models in order to achieve a numerically efficient optimization procedure. Also, we ensure manufacturability through minimum length-scale constraints.

The manuscript is organized as follows. Section 2 summarizes the working principle of MEMS gyroscopes and their design requirements. Also, it introduces the considered design problems for the single mass and the tuning resonators, followed by the employed physical models and model reduction techniques. The proposed topology optimization approach is presented in Section 3, discussing the employed regularization strategies, material properties interpolation and optimization problem formulations, as well as the choice of the algorithm parameters. Section 4 presents and discusses the optimization results for the single mass and tuning fork MEMS resonator layouts, as well as their validation with full model simulations. Finally, Section 5 concludes the paper with a summary of the obtained findings.

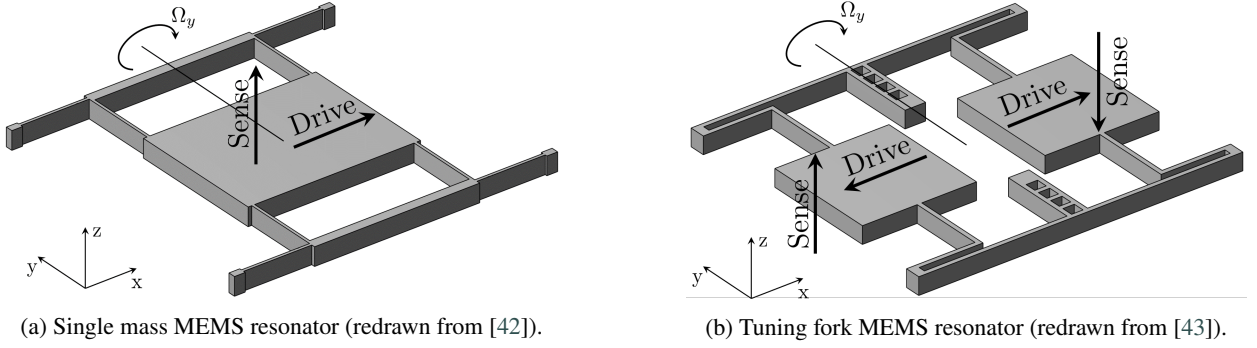


Figure 1: Schemes of MEMS resonators configurations for gyroscope applications.

2. MEMS resonators modelling

In this paper we present a design methodology for the synthesis of industrially relevant MEMS resonators, based on topology optimization. The proposed method is applicable to general low frequency resonators in which suspended proof masses or plates are employed, and where both flexural and torsional modes are of interest: typical examples are inertial sensors (i.e. accelerometers and gyroscopes) or scanning micromirrors. In the discussion we will focus on both simple single mass and coupled tuning fork MEMS resonators, and we will consider, as a relevant practical example, the application to MEMS gyroscopes.

In this Section, we will briefly recap the working principle of single mass and tuning fork MEMS gyroscopes, summarizing their design requirements and introducing the considered model problems, i.e. the geometric layout, design domains, anchoring, etc. This is followed by a discussion of the employed physical models, in terms of finite element method and model reduction techniques.

2.1. Model problems: single mass and tuning fork MEMS gyroscopes

MEMS gyroscopes are microsensors that are able to detect an external angular rate by exploiting the Coriolis effect. Possible mechanical layouts of such devices for the detection of the angular rate Ω_y around the y axis are presented in Figure 1. In the single mass layout (Figure 1a), a harmonic oscillation is imposed to a suspended proof mass along the x "drive" direction. In presence of an external angular rate Ω_y , a sinusoidal Coriolis force, proportional in amplitude to Ω_y , is induced at the drive frequency along the z "sense" direction. This eventually causes a sinusoidal displacement along z , which, again, is proportional in amplitude to Ω_y and can be used as an indirect measure of the external angular rate. All single mass MEMS gyroscopes suffer from several shortcomings and therefore have limited practical relevance. Most of these can be overcome by the introduction of additional masses.

The tuning fork architecture (Figure 1b) is used to increase the robustness against external inertial inputs, such as accelerations, shocks (jerks) and vibrations, that can easily degrade the detection of the small Coriolis induced displacement. By employing two coupled identical masses driven in anti-phase along x , two anti-phase Coriolis forces are generated along z in presence of an external angular rate Ω_y . Using differential sensing it is possible to preserve the only signal of the Coriolis induced displacement, while possible effects of "common mode" inputs, providing in-phase excitation to the proof masses, is automatically canceled.

In the design of industrial type MEMS gyroscopes, the drive natural frequency ω_d is usually chosen to be around 20–30 kHz, in order to better compensate external disturbances related to sound and vibrations, and to guarantee the coupling with the electronic circuit that actuates the drive motion with constant frequency and amplitude [7]. The sense natural frequency ω_s is instead kept at a 2%-10% frequency mismatch $\Delta\omega = \omega_s - \omega_d$ from the drive one. This is done as a trade off between obtaining adequate amplification of the Coriolis response close to the drive resonance and ensuring minimum system sensitivity to variations in resonant frequencies or damping properties [7]. In addition, in order to make the structure stiff enough to prohibit other unwanted motions, the natural frequencies associated with spurious motions, i.e. all modes different than the drive or sense ones, have to be kept as high as possible, usually at least 10%-15% higher than ω_s .

Due to the extreme level of design freedom introduced by the topology optimization approach, it is of utmost importance to ensure that the optimization addresses the right question. The first issue is therefore to determine which

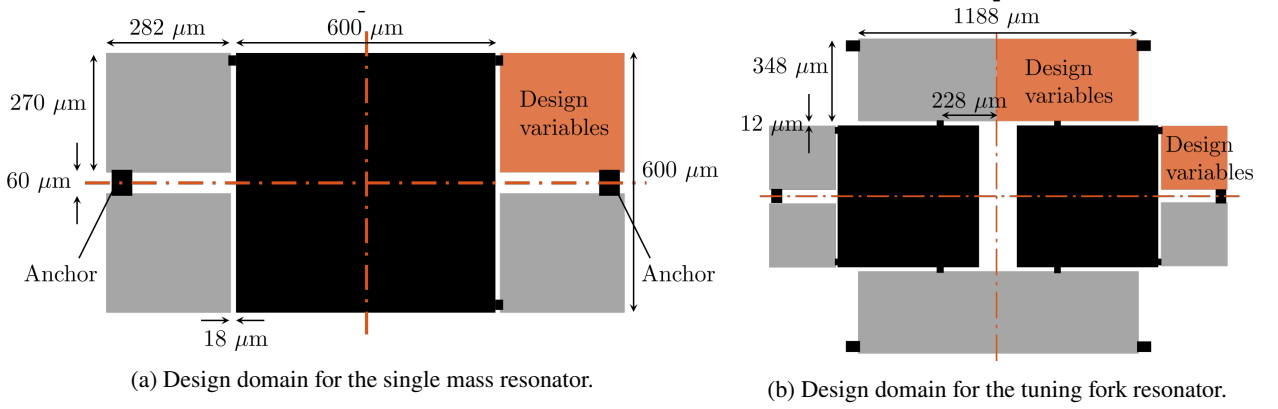


Figure 2: Setup of the design domains for the considered MEMS resonator design cases.

parts should be designable and which should be kept fixed. In this work, we choose to devote our attention to the design of the connecting springs, and hence, keep both proof masses and anchor points fixed. With this in mind, the considered design domains for the single mass and the tuning fork MEMS resonators are as shown in Figure 2. For what concerns the single mass resonator (Figure 2a), the considered design includes a $600 \mu\text{m} \times 600 \mu\text{m}$ squared proof mass and four $282 \mu\text{m} \times 270 \mu\text{m}$ symmetric design domains for the suspending structures. The connections between the proof mass and the suspending structures are located at the corners of the proof mass, while one anchor is placed on each side of the proof mass. In the case of the tuning fork resonator (Figure 2b), two square proof masses with the same $600 \mu\text{m} \times 600 \mu\text{m}$ dimensions as in the single mass case are considered, each one connected to two design domains for the suspending springs with the same configuration as the single mass case. In addition, two $1080 \mu\text{m} \times 348 \mu\text{m}$ design domains are considered for the structure that couples the motion of the two proof masses. For both the suspending and the coupling structures, the anchors have been placed as far as possible from the connections to the proof masses, in order to have sufficient design space to obtain adequately compliant structures. The material properties of polysilicon are considered in the design, i.e. a Young modulus of $E_0 = 148000 \text{ MPa}$, a Poisson ratio of $\nu = 0.23$ and a mass density of $\rho_0 = 2330 \text{ kg/m}^3$. Also, an out-of-plane thickness of the MEMS structures equal to $25 \mu\text{m}$ is chosen.

2.2. Physical models

The in-plane and out-of-plane motion of the planar MEMS geometries in Figure 2 is in this work modelled using four-node linear quadrilateral Mindlin shell finite elements [44]. Elements of this type have been chosen as they provide a satisfying compromise between results accuracy and computational costs. Extensive numerical experiments have in fact shown that in order to improve the accuracy e.g. with linear brick hexahedral elements, at least 4 elements along the out of plane thickness of the structure have to be considered, and this would lead to a too high computational cost for our optimization purposes, and easily also to memory saturation issues for the considered 16 GB RAM.

In order to ensure efficient, yet accurate, analysis results while maintaining an adequate design freedom for the topology optimization procedure, it is generally desirable to use a sufficiently fine mesh for the design domains, whereas the mesh of the remaining parts should be kept as coarse as possible. With this in mind the structural domains are discretized by quadrilateral finite elements as seen in Figure 3. In particular, a coarse structured mesh with $15 \mu\text{m} \times 15 \mu\text{m}$ elements is considered inside the proof mass, while a fine structured mesh with $1.5 \mu\text{m} \times 1.5 \mu\text{m}$ elements is associated with the design domains of the suspending and coupling structures to be optimized. In the transition zone between the two structured meshes with different element dimensions, a free mesh is used. The proposed choice of the mesh setup has proven to be a good compromise between reducing the computational cost and keeping a good model accuracy: in general, no relevant deformations are expected inside the proof mass for the modes of interest, i.e. the first ones, that are usually associated with quasi-rigid translations of the proof masses [25]. In order to accurately model possible significant local deformations, we note that the fine structured mesh setup is considered also in the portions of the proof masses that are close to the connections to the suspending/coupling structures.

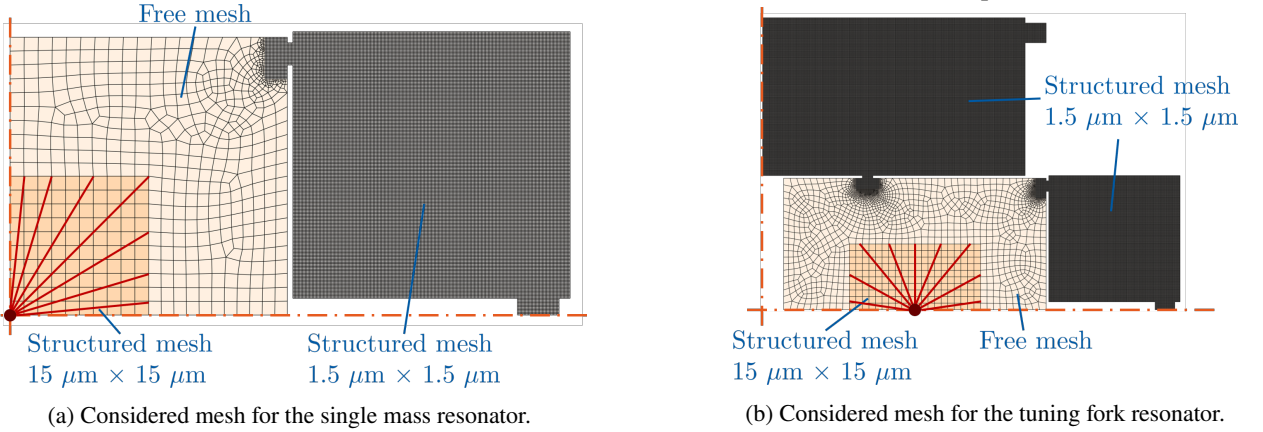


Figure 3: Mesh setup for the considered MEMS resonator design cases.

2.2.1. Finite element formulations

In general, the design problems in this work are solved using linear Mindlin quadrilateral shell elements. However, considering the planar geometry of the MEMS resonator, the in-plane and the out-of-plane degrees of freedom of the structure can be decoupled, i.e. it is possible to analyze them separately, and hence significantly reduce the computational cost. Therefore, the in-plane dynamics of the MEMS structure are analyzed through linear isoparametric quadrilateral finite elements [44], with 4 nodes per element and two degrees of freedom per node, i.e. the displacements u_x and u_y along the x and y directions. The out-of-plane dynamics are instead analyzed through linear quadrilateral isoparametric Mindlin plate finite elements, with 4 nodes per element and three degrees of freedom per node, i.e. the displacement u_z along the z direction, and rotations θ_x and θ_y around the x and y axes. In particular, reduced numerical integration is performed to compute the shear stiffness terms of the Mindlin plates, in order to avoid shear locking effects [44]. The formulation of the finite elements have been implemented in Matlab and validated through comparison of the results with Abaqus commercial software.

Using this approach leads to the following undamped, linear equations of motion:

$$\mathbf{M}\ddot{\mathbf{u}} + \mathbf{K}\mathbf{u} = \mathbf{f} \quad (1)$$

where \mathbf{K} and \mathbf{M} are the stiffness and mass matrices, respectively, \mathbf{u} is the full vector of degrees of freedom, $\ddot{\mathbf{u}}$ are the accelerations and the vector \mathbf{f} contains general nodal forces, i.e. applied external loads and/or reaction forces.

Since the main goal of the considered MEMS resonator design problem is to tune the first set of natural frequencies ω_i and their associated modes shapes Φ_i , the problem is recast as the following undamped eigenvalue problem:

$$(-\omega_i^2 \mathbf{M} + \mathbf{K})\Phi_i = \mathbf{0} \quad (2)$$

We remark that no damping terms are present in Eq. (1) and (2), which is deemed acceptable since MEMS gyroscopes usually operate at very low pressure and very low non-dimensional damping ratios (in the order of 10^{-3}) [7]. Therefore the computed undamped natural frequencies will be representative of the resonant frequencies in real working conditions.

The main bottleneck in any structural optimization method concerns the repeated finite element analysis needed for the iterative design update process. Therefore it is crucial to make the analysis as fast as possible to ensure a useful and efficient design approach. In this framework, reduced order models (ROMs) are more and more frequently used to speed up the dynamic analyses of MEMS resonators, both in linear [45, 25] and nonlinear [46, 47, 48] regimes. In the following, a combination of multi-point constraints, static approximations and static reduction will be used.

2.2.2. Reduced order modelling

Following the observation from [41, 25], good approximate solutions of Eq. (2) can be obtained with reduced computational cost, assuming that the first natural modes are mainly associated with quasi-rigid motions of the proof masses and quasi-static deformations of the suspending/coupling structures, with negligible effects of their internal dynamics. This assumption will be used to introduce reduced order models in the computation.

As first step, we represent the quasi-rigid motion of the proof masses by additional nodes, placed at their centers and associated with 6 degrees of freedom in space (cf. red dots in Figure 3). Such additional nodes are rigidly connect to the inner nodes of the proof masses (cf. Figure 3) through *multipoint constraints* (MPC, [44]), that result in a transformation equation from the full set of degrees of freedom \mathbf{u} to a smaller vector of retained degrees of freedom \mathbf{u}_m (cf. Appendix A):

$$\mathbf{u} = \mathbf{T}_m \mathbf{u}_m \quad (3)$$

Eq. (3) can be substituted into Eq. (1), and after premultiplying by \mathbf{T}_m^T we get the equations of motion in terms of the only retained degrees of freedom:

$$\mathbf{M}_m \ddot{\mathbf{u}}_m + \mathbf{K}_m \mathbf{u}_m = \mathbf{f}_m \quad \text{where:} \quad \mathbf{K}_m = \mathbf{T}_m^T \mathbf{K} \mathbf{T}_m \quad \mathbf{M}_m = \mathbf{T}_m^T \mathbf{M} \mathbf{T}_m \quad \mathbf{f}_m = \mathbf{T}_m^T \mathbf{f} \quad (4)$$

The MPC are used for both the single mass and the tuning fork resonators. For what concerns the single mass resonator, we assume that the first natural modes are associated with quasi-rigid displacements of the proof mass along its 6 degrees of freedom. We therefore estimate the first mode shapes by imposing unitary displacements along these 6 directions, and solving the related linear static problem while imposing proper boundary conditions related to the fixed anchor regions. Once the static deformation is computed, the i -th natural frequency is estimated from the computation of the mass and the stiffness associated with the estimated mode shape. Therefore, for the single mass layout we employ this *static approximation* of the eigenfrequencies:

$$\tilde{\omega}_i = \sqrt{\frac{\tilde{k}_{m,i}}{\tilde{m}_{m,i}}} = \sqrt{\frac{\tilde{\Phi}_{m,i}^T \mathbf{K}_m \tilde{\Phi}_{m,i}}{\tilde{\Phi}_{m,i}^T \mathbf{M}_m \tilde{\Phi}_{m,i}}} \quad \text{where:} \quad \mathbf{K}_m \tilde{\Phi}_{m,i} = \mathbf{f}_{m,i} \quad (5)$$

In Eq. (5) $\tilde{\omega}_i$ and $\tilde{\Phi}_{m,i}$ are the estimations of the eigenfrequencies and the eigenmodes, while $\tilde{k}_{m,i}$ and $\tilde{m}_{m,i}$ are the estimations of the modal stiffness and mass. Since no external load is applied in the estimation of the i -th mode shape, the load vector $\mathbf{f}_{m,i}$ contains the reaction forces for the considered static load case with imposed displacements.

In the case of the tuning fork resonator, it is more difficult to a priori guess the first mode shapes, due to the the presence of the coupling springs between the two proof masses. We therefore first statically reduce the set \mathbf{u}_m of 2.8 millions degrees of freedom to a set \mathbf{u}_r of 12 degrees of freedom related to the two centers of the proof masses, and then solve the eigenvalue problem on the reduced system. The *static reduction* exploits the following transformation equation (cf. Appendix A):

$$\mathbf{u}_m = \mathbf{T}_r \mathbf{u}_r \quad (6)$$

Substituting Eq. (6) into Eq. (4) and premultiplying by \mathbf{T}_r^T , we get:

$$\mathbf{M}_r \ddot{\mathbf{u}}_r + \mathbf{K}_r \mathbf{u}_r = \mathbf{f}_r \quad \text{where:} \quad \mathbf{K}_r = \mathbf{T}_r^T \mathbf{K}_m \mathbf{T}_r \quad \mathbf{M}_r = \mathbf{T}_r^T \mathbf{M}_m \mathbf{T}_r \quad \mathbf{f}_r = \mathbf{T}_r^T \mathbf{f}_m \quad (7)$$

The estimated natural frequencies are finally obtained by solving the small eigenvalue problem on the reduced system:

$$(-\tilde{\omega}_i \mathbf{M}_r + \mathbf{K}_r) \Phi_{r,i} = \mathbf{0} \quad (8)$$

The presented reduced order models will be used in the optimization to efficiently estimate the resonator natural frequencies. In particular, the accuracy and computational cost of the employed ROMs will be assessed through a comparison of the results with the full eigenvalue problem (Eq. (2)).

3. Topology optimization

The topology optimization problem is formulated exploiting the density method, where one design variable $\gamma_e \in \{0, 1\}$ is assigned to each finite element, in order to describe the material distribution in the design space with a scaling of the properties of each finite element between void and solid (0 = void, 1 = solid). Intermediate values are permitted during the optimization process, but are penalized in order to ensure all elements are 0 or 1 in the final design: this is done relying on appropriate regularization by filtering/projection techniques and length-scale control, and particular interpolation functions of the material properties. In this Section we will discuss the employed regularization strategies, followed by the optimization problem formulations.

3.1. Regularization and interpolation of material properties

The filtering and projection scheme from [49] is adopted: starting from the design variables γ_e , the filtered variables $\tilde{\gamma}_e$ are obtained by a weighted average of the neighbouring elements γ_e , i.e. through a convolution type filtering function $\mathcal{F}(\gamma_{e,j})_{j \in \mathbb{N}_{s,e}(r_{min})}$:

$$\tilde{\gamma}_e = \mathcal{F}(\gamma_{e,j})_{j \in \mathbb{N}_{s,e}(r_{min})} = \frac{\sum_{j \in \mathbb{N}_{s,e}(r_{min})} w(x_j) v_j \gamma_{e,j}}{\sum_{j \in \mathbb{N}_{s,e}(r_{min})} w(x_j) v_j} \quad (9)$$

where v_j is the volume of the j -th element and $\mathbb{N}_{s,e}(r_{min})$ is the set of neighbouring elements, defined as the set of elements lying within a circle with radius r_{min} centered on element e . The linear weighting function $w(x_j)$ is given as:

$$w(x_j) = r_{min} - |x_j - x_e| \quad (10)$$

A smoothed Heaviside projection [49] is employed to address convergence to a solid/void solution: the projected design variables (or physical densities) $\bar{\gamma}_e$ are computed through the following smoothed Heaviside function $\mathcal{H}(\tilde{\gamma}_e, \eta, \beta)$ [49], shown in Figure 4a:

$$\bar{\gamma}_e = \mathcal{H}(\tilde{\gamma}_e, \eta, \beta) = \frac{\tanh(\beta\eta) + \tanh(\beta(\tilde{\gamma}_e - \eta))}{\tanh(\beta\eta) + \tanh(\beta(1 - \eta))} \quad (11)$$

where β is the sharpness parameter controlling the slope of the projection and η is the location of the threshold. The threshold is here set to $\eta = 0.5$, while β is increased incrementally during the optimization process.

The projected design variables are then used to interpolate the material properties of the elements between solid and void: as shown in Figure 4b, we here use a Rational Approximation of Material Properties (RAMP) model to interpolate the stiffness properties [50], and a linear interpolation for the mass properties. The Young modulus E_e and the mass density ρ_e for a generic element e with physical density $\bar{\gamma}_e$ will be:

$$E_e = E_{min} + \frac{\bar{\gamma}_e}{1 + q(1 - \bar{\gamma}_e)} (E_0 - E_{min}) \quad \rho_e = \rho_{min} + \bar{\gamma}_e (\rho_0 - \rho_{min}) \quad (12)$$

where E_0 and ρ_0 are the modulus and mass density of the considered material, while $E_{min} = 10^{-8} \cdot E_0$ and $\rho_{min} = 10^{-7} \cdot \rho_0$ are small values assigned to void elements, in order to avoid singular element matrices. The choice of a RAMP interpolation for stiffness properties, combined with a linear mass density interpolation, allows to avoid numerical artifacts, such as artificial localized modes in low density areas related to SIMP interpolation [51]. In particular, we use $q = 4$ in Eq. (12).

Geometric constraints allow to impose a minimum length-scale for the optimized layouts, namely a minimum width for the geometric features. Their formulation follows the one proposed in [52]. In order to formulate the geometric constraints, two structural indicator functions I^s and I^v are defined to capture the inflection regions of the solid and

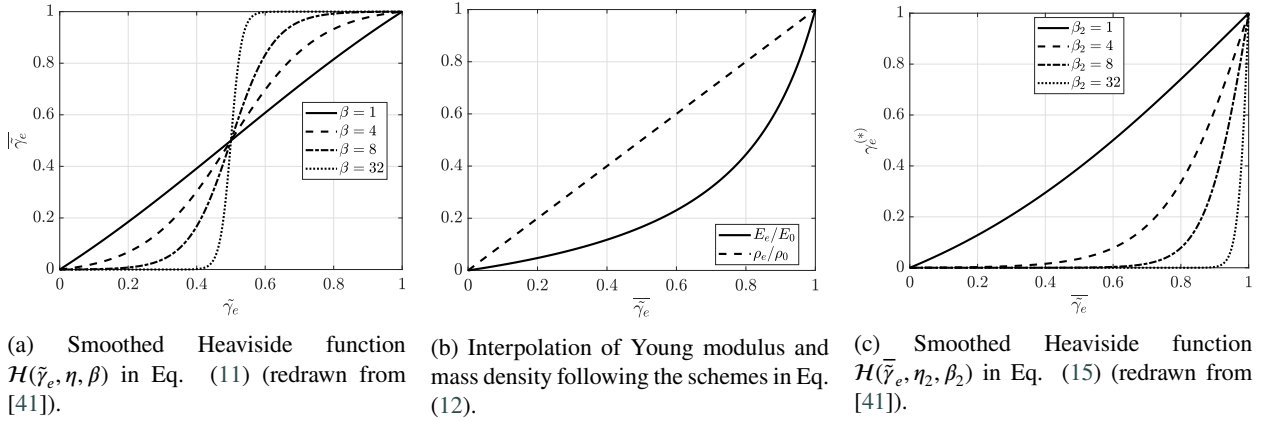


Figure 4: Plots of the functions in Eqs. (11), (12) and (15).

void phases respectively:

$$\begin{aligned}
 I^s &= \tilde{\gamma} \cdot \exp(-c \cdot \|\nabla \tilde{\gamma}\|^2) \\
 I^v &= (1 - \tilde{\gamma}) \cdot \exp(-c \cdot \|\nabla \tilde{\gamma}\|^2) \\
 \text{with: } c &= r_{min}^4
 \end{aligned} \tag{13}$$

Based on the indicator functions, the geometric constraints are imposed as:

$$\begin{aligned}
 g^s &= \frac{1}{n} \sum_{i \in \mathbb{N}} I_i^s \cdot [\min\{(\tilde{\gamma}_i - \eta_e), 0\}]^2 \leq \varepsilon_{gc} \\
 g^v &= \frac{1}{n} \sum_{i \in \mathbb{N}} I_i^v \cdot [\min\{(\eta_d - \tilde{\gamma}_i), 0\}]^2 \leq \varepsilon_{gc}
 \end{aligned} \tag{14}$$

where n is the total number of elements in the discretization set \mathbb{N} , $\eta_d = 0.25$ and $\eta_e = 1 - \eta_d = 0.75$ are set to impose a minimum length scale corresponding to the filter radius r_{min} [49], and ε_{gc} is a given tolerance.

Convergence to black and white layouts is addressed by applying explicit grey penalization constraints as proposed in [41]. The main idea is that, if grey connections are present in the structure, pushing grey variables towards void causes disconnections, and local stiffness or eigenfrequencies approach zero. The use of grey connections can be therefore discouraged by bounding this change in the local stiffness or in the eigenfrequencies. It is therefore useful to define a new field of variables $\gamma_e^{(*)}$, in which intermediate design variables are pushed towards void by applying an additional projection on the projected field $\tilde{\gamma}_e$. Thus, we define the following projection shown in Figure 4c:

$$\gamma_e^{(*)} = \mathcal{H}(\tilde{\gamma}_e, \eta_2, \beta_2) \tag{15}$$

where the new threshold and sharpness parameter are set to $\eta_2 = 1$ and $\beta_2 = 3\beta$ respectively.

In the case of the single mass resonator, the new estimations of the drive and y-motion natural frequencies $\tilde{\omega}_d^{(*)}$ and $\tilde{\omega}_y^{(*)}$ are computed for the structure defined by the new field of variables $\gamma_e^{(*)}$. In order to bound their difference with respect to the original eigenfrequencies estimations $\tilde{\omega}_d$ and $\tilde{\omega}_y$, the following constraints are imposed:

$$1 - \frac{\tilde{\omega}_d^{(*)}}{\alpha_{grey} \cdot \tilde{\omega}_d} \leq 0, \quad 1 - \frac{\tilde{\omega}_y^{(*)}}{\alpha_{grey} \cdot \tilde{\omega}_y} \leq 0 \tag{16}$$

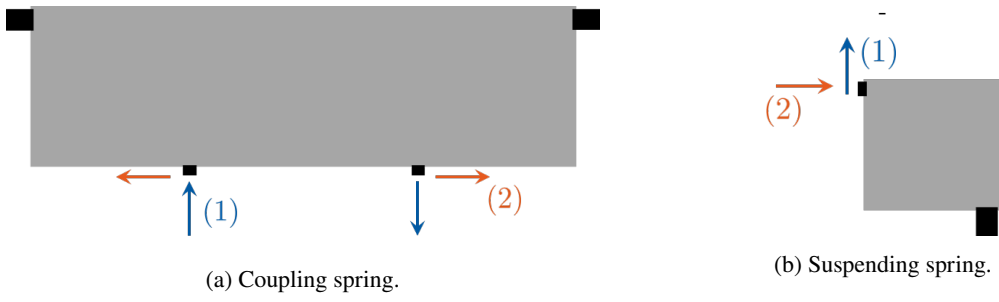


Figure 5: Additional load cases employed for grey penalization in the tuning fork MEMS resonator.

where the lower bound parameter is set to $\alpha_{grey} = 0.35$.

In the case of the tuning fork resonator, two different sets of springs (coupling and suspension) are present, and therefore preventing $\tilde{\omega}_d^{(*)}$ and $\tilde{\omega}_y^{(*)}$ from going to zero still allows the presence of grey elements or even disconnections in one of the two springs, provided that the other spring is stiff enough. In order to apply grey penalization constraints independently to the two springs, we instead consider the stiffness of each spring to two unitary static imposed in-plane displacements, as depicted in Figure 5. Such displacements are applied to the sections at which each spring connects to the proof masses, and correspond to one vertical (1) and one horizontal (2) displacement at the single connection of the suspending spring, and to two couples of antiphase vertical (1) and horizontal (2) displacements respectively at the two connections of the coupling spring. After imposing the boundary conditions related to the fixed anchor regions, the stiffness k_{ij} of the i -th spring subjected to the j -th displacement can be found as:

$$k_{ij} = \mathbf{f}_{ij}^T \mathbf{u}_{ij} \quad \text{with: } \mathbf{K}_i \mathbf{u}_{ij} = \mathbf{f}_{ij} \quad (17)$$

i.e. solving a linear problem, where \mathbf{K}_i is the stiffness matrix associated with the i -th spring design domain, while \mathbf{u}_{ij} and \mathbf{f}_{ij} are displacement and load vectors. The grey penalization constraints are imposed by bounding the change of each k_{ij} when applying the additional projection in Eq. (15):

$$1 - \frac{k_{ij}^{(*)}}{\alpha_{grey}^2 \cdot k_{ij}} \leq 0 \quad (18)$$

where α_{grey}^2 is used to properly scale the constraints from Eq. (16) to Eq. (18) when focusing on stiffness instead of eigenfrequency.

3.2. Optimization formulation

In the following, the formulations of the topology optimization problems for the design of the single mass and the tuning fork MEMS resonators are discussed. We will first assess the suitability of the method with the design of single mass resonators, and we will then approach the design of tuning fork resonators.

3.2.1. Design of the single mass MEMS resonator

For the single mass resonator, a similar formulation to the one presented in [41] is considered:

$$\begin{aligned}
 \min_{\gamma_e} \quad & \text{Vol} = \frac{\sum_e \bar{\gamma}_e v_e}{\sum_e v_e} \\
 \text{subject to} \quad & \frac{(\tilde{\omega}_d - \omega_{d,des})^2}{\omega_{d,des}^2} - \epsilon^2 \leq 0 \\
 & \frac{(\tilde{\omega}_s - \omega_{s,des})^2}{\omega_{s,des}^2} - \epsilon^2 \leq 0 \\
 & \frac{1.2 \cdot \tilde{\omega}_s}{\tilde{\omega}_{sp}} - 1 \leq 0 \\
 & \omega_{d,des} = 0.95 \cdot \omega_{s,des} \\
 & \tilde{\omega}_i = \sqrt{\frac{\tilde{k}_{m,i}}{\tilde{m}_{m,i}}} = \sqrt{\frac{\tilde{\Phi}_{m,i}^T \mathbf{K}_m \tilde{\Phi}_{m,i}}{\tilde{\Phi}_{m,i}^T \mathbf{M}_m \tilde{\Phi}_{m,i}}} \\
 & \mathbf{K}_m \tilde{\Phi}_{m,i} = \mathbf{f}_{m,i}, \quad i = d, s, sp \\
 & \text{Geometric constraints} \\
 & \text{Grey penalization constraints}
 \end{aligned} \tag{19}$$

The objective function to be minimized is the amount of used material Vol : besides leading to a lightweight suspending structure, this in particular helps the convergence of the algorithm to a feasible layout, avoiding undesired big portions of material attached to the suspending structure that are associated with low-frequency local spurious modes. A set of constraints are imposed to match the desired target drive and sense natural frequencies $\omega_{d,des}$ and $\omega_{s,des}$ with a certain relative tolerance ϵ , and to satisfy a 5% mismatch. The first spurious frequency $\tilde{\omega}_{sp}$ is kept at least 20% higher than the sense frequency as marked in blue in Eq. (19). We note that with respect to [41] we have reduced the desired distance of the first spurious mode from 40% to 20%: a slight relaxation of constraints, still in accordance with usual industrial requirements (cf. Section 2), is needed to achieve feasible layouts when considering also out of plane dynamics. The remaining constraints of the formulation are associated with the static estimation of the natural frequency, and to geometric and grey penalization constraints.

We remark that for the considered design case of the single mass resonator the drive and sense modes are associated with x and z motions of the proof mass respectively, while the first spurious mode is the one with the lowest frequency among the remaining ones, associated with the other 4 degrees of freedom of the proof mass.

3.2.2. Design of the tuning fork MEMS resonator

The formulation of the topology optimization problem for the tuning fork resonator design directly follows from the one of the single mass resonator:

$$\begin{aligned}
 \min_{\gamma_e} \quad & \text{Vol} = \frac{\sum_e \bar{\gamma}_e v_e}{\sum_e v_e} \\
 \text{subject to} \quad & \frac{(\tilde{\omega}_d - \omega_{d,des})^2}{\omega_{d,des}^2} - \epsilon^2 \leq 0 \\
 & \frac{(\tilde{\omega}_s - \omega_{s,des})^2}{\omega_{s,des}^2} - \epsilon^2 \leq 0 \\
 & 1 - \frac{0.8 \cdot \tilde{\omega}_s}{\tilde{\omega}_{s,sp}} \leq 0 \\
 & \frac{1.15 \cdot \tilde{\omega}_s}{\tilde{\omega}_{sp}} - 1 \leq 0 \\
 & \omega_{d,des} = 0.95 \cdot \omega_{s,des} \\
 & (-\tilde{\omega}_i \mathbf{M}_r + \mathbf{K}_r) \Phi_{r,i} = \mathbf{0} \\
 & \text{Geometric constraints} \\
 & \text{Grey penalization constraints}
 \end{aligned} \tag{20}$$

Besides the different reduced order model for the computation of the natural frequencies, a slight modification of the formulation is performed to manage the different nature of spurious modes in the tuning fork resonator. In this case it is in fact not possible to move all the spurious modes to high frequencies: we therefore impose that the frequency $\tilde{\omega}_{s,sp}$ of the "spurious sense" mode, i.e. the one with in-phase z motion of the masses, is sufficiently lower (15%) than the drive one. Also, in this case the first spurious frequency $\tilde{\omega}_{sp}$ after the spurious sense one is desired to be at least 15% higher than the sense natural frequency.

3.3. Details of the optimization algorithm

We will now discuss the details of the proposed optimization algorithm, whose scheme is presented in Fig. 6.

The procedure starts with the initialization of the design variables to an intermediate value $\gamma_e = 0.4$. At each optimization iteration, the filtering and the projection schemes are applied, and the needed finite element analyses are performed. Then, the values of the objective function and the constraints are computed, together with their sensitivity to variations in the design variables. This allows to use the Method of Moving Asymptotes (MMA) [53] as the gradient-based optimizer that provides an updated design variables field. The finite element analyses followed by the sensitivity analysis are performed again on this new structure to obtain a new updated design variables field by MMA. The process is repeated until specific stopping criteria are satisfied [41].

For what concerns the parameters introduced in the previous Sections, the following rules are employed for their setting. The filter radius is set to $r_{min} = 4$ elements, that with the chosen discretization allows to impose a minimum length-scale of $6 \mu\text{m}$ to the optimized geometric features. A continuation scheme is applied to the sharpness parameter β of the projection scheme and to the tolerances ϵ and ϵ_{gc} , to gradually enforce a black and white layout that satisfies the constraints with the desired tolerances. In particular, the desired tolerance ϵ for the constraints on the target frequencies is set to $3 \cdot 10^{-4}$, while the tolerance ϵ_{gc} for the geometric constraints is decreased during the optimization as the projection parameter β increases, as described in [41]. Starting from $\beta = 1$, the projection parameter is kept constant for 50 iterations and then increased by a factor 1.2 when the constraints are satisfied with a tolerance of $2 \cdot 10^{-4}$. When β changes, constraints are slightly relaxed increasing the tolerances ϵ and ϵ_{gc} by a factor of 100 and decreasing them back to their desired values through 13 iterations. The process is then repeated increasing β each time by a factor of 1.2 up to $\beta = 32$: this value of β allows to reach a measure of non-discreteness in the solution [54] $M_{nd} \leq 1\%$ and therefore a satisfying black and white level of the solution. We note that the optimization parameters have been chosen based on exhaustive numerical experiments.

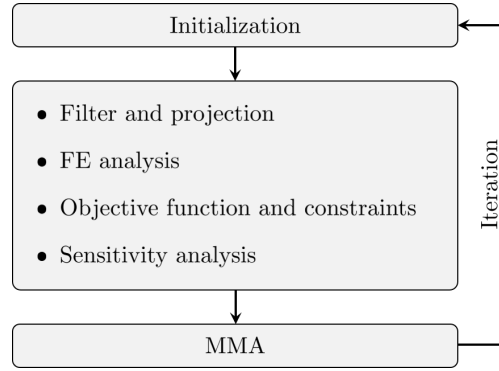


Figure 6: Scheme of the proposed topology optimization algorithm.

As underlined in [52], the application of geometric constraints is effective after an initial topology has formed. For this reason, they are introduced later into the topology optimization process, for $\beta > 7$, while grey penalization constraints are active from the beginning of the optimization procedure.

The needed FEM solvers implemented in MATLAB: eigenvalue problems are solved by ARPACK (as "eigs"), applying an implicitly restarted Lanczos method (IRLM), whereas linear problems are solved applying LU decomposition (as "\"). Due to the planar geometry of the structure, in-plane and out-of-plane dynamics are decoupled and it is possible to solve Eq. (5) and (8) separately for in-plane and out-of-plane degrees of freedom. This significantly reduces the overall computational cost of the procedure.

The formulated optimization problems are solved for local optimality using the Method of Moving Asymptotes (MMA) by Svanberg [53] as a gradient-based optimizer. This requires the sensitivities of the objective function and the constraints with respect to changes in the design variables. In general, the sensitivities of the functions that depend only on the design field can be easily computed by analytically differentiating their expressions. On the other hand, the sensitivities of the functions that depend on the state of the system can be computed exploiting the adjoint method, since many design variables are considered. The majority of the sensitivities of interest are taken from [41], while the main differences with respect to this reference are presented in Appendix B.

Finally, we note that no critical numerical issues related to repeated eigenvalues were encountered in the optimization, and therefore no particular counteractions have been considered. We believe that this is related to the choice of the treated optimization problems, that help in maintaining the eigenvalues of interest well separated and avoiding the lack of differentiability discussed in [55].

4. Results and discussion

In this Section, the optimization results for the single mass and tuning fork MEMS resonators design cases are presented and discussed, and the introduced reduced order models are validated comparing the simulation results with the ones obtained with the full models.

4.1. Optimization of the single mass resonator

The single mass resonators are optimized for different industrially acceptable target sense natural frequencies $f_{s,des} = 16$ kHz, 24 kHz, 32 kHz, 40 kHz, and the optimized layouts are shown in Figure 7. The drive, sense and first spurious modal shapes of the different optimized layouts are shown in Figures 8, 9, 10, 11. In particular, it can be seen how the first spurious mode is associated with an in-plane y motion of the proof mass (Figures 8c, 9c, 10c, 11c).

Referring to Figure 7, the optimized layouts for the single mass resonator show different configurations of the suspending spring, depending on the target natural frequencies. For the lowest target natural frequency, i.e. $f_{des} = 16$ kHz, the layout shows a thin, S-shaped, suspending spring (Figure 7a). When increasing the target natural frequencies, the spring meandering reduces and its thickness increases in order to achieve a lower compliance, and the layouts therefore evolve towards the thick, L-shaped, suspending spring reached for $f_{s,des} = 40$ kHz (Figure 7d). All the four designed layouts present slots in the springs: removing material from the most rigid locations, that have a low impact

on the overall compliance, allows the optimizer to minimize the amount of used material while maintaining the desired natural frequencies.

In summary, the optimization problem formulation in Eq. (19) is found to be capable of producing single mass resonator designs that match all desired target frequency constraints when starting from an uniform initial configuration.

4.2. Optimization of the tuning fork resonator

The tuning fork resonators are again optimized for $f_{s,des} = 16$ kHz, 24 kHz, 32 kHz, 40 kHz. The optimized layouts are shown in Figures 12, while the modal shapes of the sense spurious, drive, sense and first spurious modes are shown in Figures 14, 15, 16, 17. In this case it can be seen that the first spurious mode is associated with anti-phase in-plane rotations of the two proof masses (Figures 14d, 15d, 16d, 17d).

In the tuning fork design case, the formulation in Eq. (20) allows to obtain the optimized layouts shown in Figures 12c and 12d for $f_{s,des} = 32$ kHz and $f_{s,des} = 40$ kHz when starting from a uniform initial design. In general, this trivial initial guess does not always guarantee feasibility for lower target natural frequencies: for example, a feasible layout is still obtained for e.g. $f_{s,des} = 26$ kHz (Figure 13b), while for $f_{s,des} = 24$ kHz a non fully connected layout is obtained (Figure 13a). Feasible layouts at low frequencies can be simply obtained by a smarter choice of the initial guess γ_i : we here consider a $25 \mu\text{m}$ dilation of the 26 kHz layout (Figure 13c), obtained by a $r_{min} = 25 \mu\text{m}$ filter and a subsequent ($\eta = 0.2, \beta = 32$) Heaviside projection:

$$\gamma_i = H \left(F \left(\bar{\gamma}_{e,j} \right)_{j \in \mathbb{N}_{s,e}(25 \mu\text{m})}, 0.2, 32 \right) \quad (21)$$

By starting the optimization from γ_i and from $\beta = 1.2^{11} = 7.43$, it is possible to obtain the final optimized layouts for 16 kHz and 24 kHz layouts shown in Figures 12a and 12b.

An interesting concept is exploited by the optimizer in the design of the coupling springs of the tuning fork layouts. That is, additional beam resonators, almost parallel to the x axis, are placed to connect the two anchor points, and are connected to the proof masses by beam-like springs. This concept proves to be particularly suitable to keep the sense spurious frequency at a sufficiently low frequency: in the sense anti-phase z motion of the masses, the central part of the additional beam resonator (Figure 18a) deforms following its second out of plane mode (Figure 18b), while in the spurious sense in-phase z motion it deforms following its first out of plane mode (Figure 18c). The higher overall compliance of the first mode in this latter case helps having an adequately low sense spurious mode frequency, as given by the design requirements (Eq. (20)).

4.3. Validation of the optimized layouts with full model simulations

In order to validate the obtained layouts and explicitly show the benefits of using reduced order models in the optimization, we finally compare the ROM results with the ones from the full model (FEVP: full eigenvalue problem in Eq. (2)), in terms of computational cost and accuracy. The comparison of computational costs is presented in Table 1, and shows how there is reduction in the time needed for eigenfrequencies computation by a factor of 7 to 8, while the total time when considering also sensitivity analysis is reduced by a factor of 2 to 3. The accuracy of the employed ROMs is validated for both the single mass and the tuning fork resonators in Tables 2 and 3 respectively, where it is shown how reduced models result to be slightly more rigid than the full ones, leading to slightly increased natural frequencies in the estimation. In particular, for in-plane motion the estimation errors are negligible, while for out-of-plane motion the errors are in the order of few percent. We also note that estimation errors increase for higher target natural frequencies: for $f_{s,des} = 40$ kHz we have a sense frequency estimation error around 3.8% for the single mass resonator, and an error around 2% for the tuning fork resonator.

Since practical situations may require a better match of the target frequencies, we propose a simple and straightforward approach to minimize the estimation error arising from the reduced order models. With this goal we run 50 further steps in the optimization when considering the full FEM problem for out of plane dynamics, i.e. excluding in this case the MPC condensation and the static approximation/reduction. To demonstrate the clean-up in frequency mismatch, we take the design with the worst frequency offset, i.e. the 40 kHz single mass in Figure 7d. The optimization process is continued for the discussed fine tuning procedure, where the out-of-plane natural frequencies are computed directly with the full eigenvalue problem (Eq. (2)), and the in-plane frequencies computation is kept with the reduced models. After fine tuning we find that the target sense frequency is perfectly matched as can be seen in the last row of

	Single mass		Tuning fork	
	ROM	FEVP	ROM	FEVP
Eigenfreq. computation	4.51 s	36.2 s	22.0 s	152 s
Sensitivity analysis	17.1 s	9.39 s	36.9 s	33.7 s
Total	21.6 s	45.5 s	58.9 s	185 s

Table 1

Comparison of the computational cost between reduced order models (ROMs) and full eigenvalue problem (FEVP), for both the single mass and the tuning fork design cases.

Table 2. Also, Figure 19 shows the introduced modifications to the structural layout: some portions of the spring are slightly enlarged by the optimizer in order to increase the overall stiffness and match $f_{s,des}$.

In summary, the proposed strategy allows to employ the computationally cheap reduced order models in most of the optimization, in order to get well performing layouts that are then fine tuned with the final 50 iterations employing the full model only for out of plane dynamics.

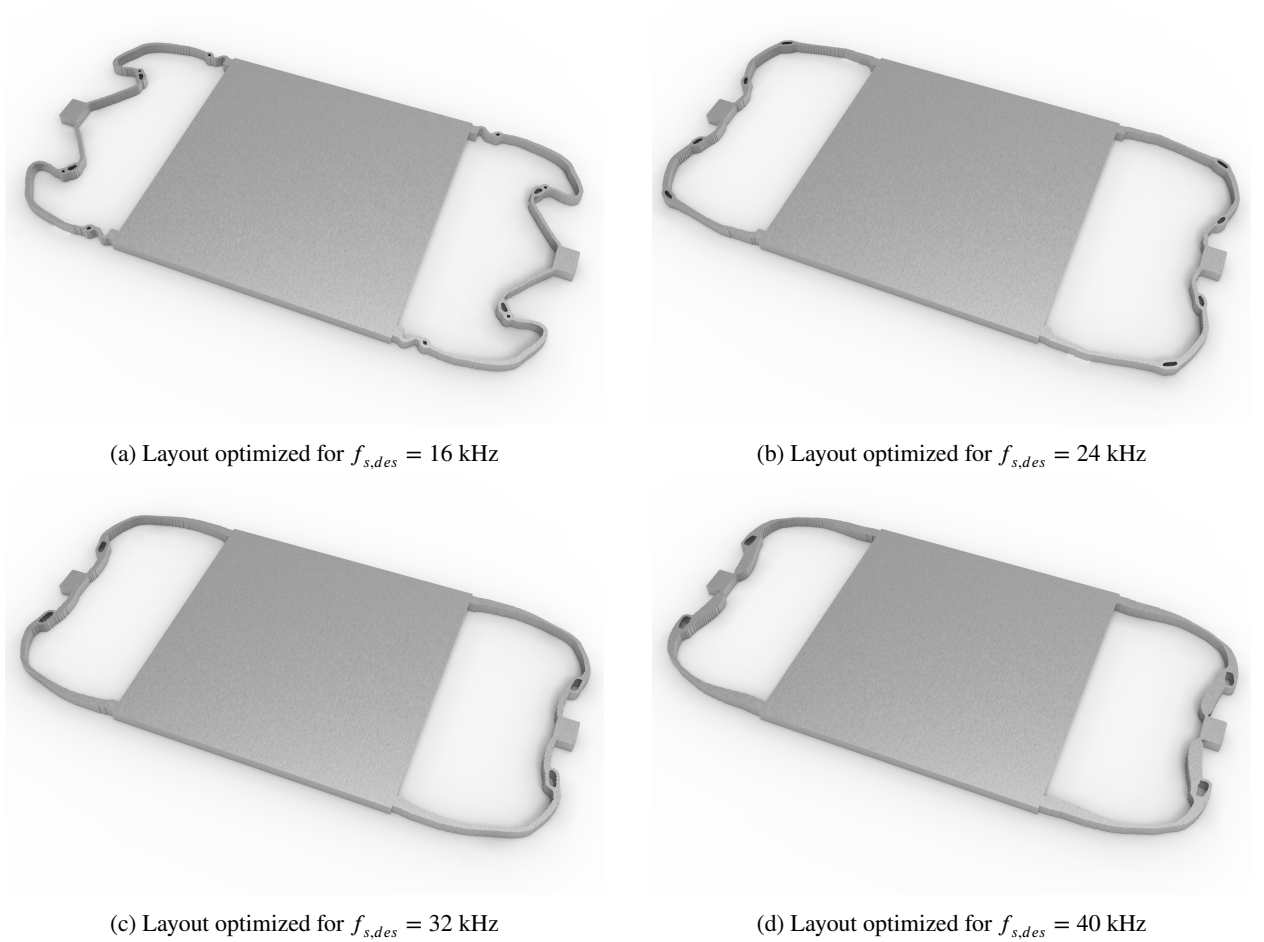
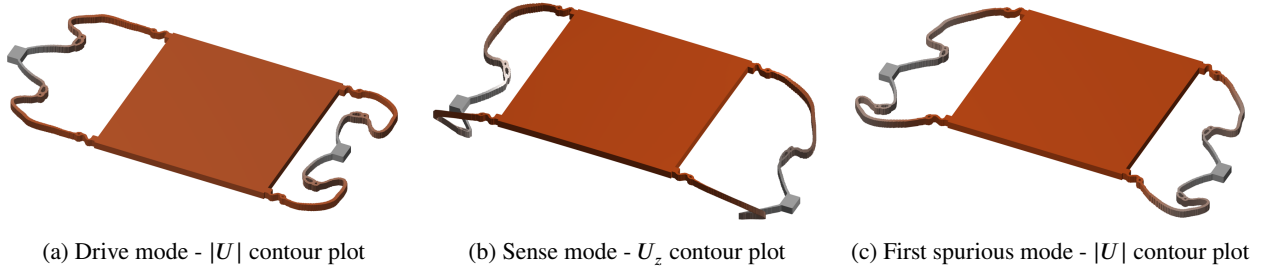
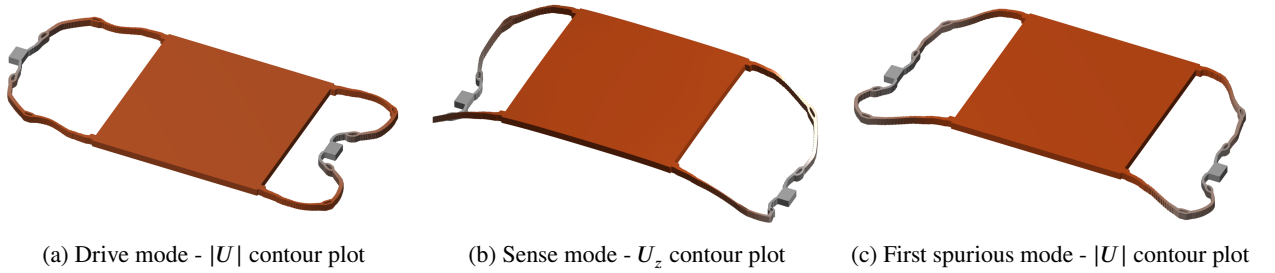
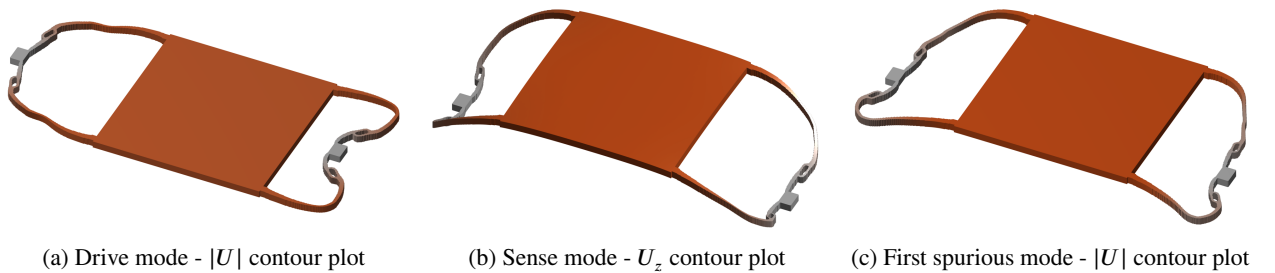


Figure 7: Single mass MEMS resonator design case: optimized layouts.

Layout	Drive eigenfreq. [Hz]			Sense eigenfreq. [Hz]			First spur. eigenfreq. [Hz]		
	ROM	FEVP	Err.	ROM	FEVP	Err.	ROM	FEVP	Err.
(a)	15195	15194	0.00%	15995	15925	0.44%	19093	19092	0.00%
(b)	22801	22800	0.00%	23996	23635	1.71%	28800	28798	0.00%
(c)	30406	30405	0.00%	31992	31117	2.81%	38394	38390	0.00%
(d)	38002	38000	0.00%	39989	38536	3.77%	48653	48647	0.01%
(d) - fine tuned	37995	37992	0.00%	-	39991	0%	54673	54664	0.01%

Table 2

Comparison between the natural frequencies obtained with the ROM and the ones obtained with the full eigenvalue problem (FEVP) for the single mass resonator optimized layouts in Figure 7. The last row is related to layout (d) after fine tuning.


Figure 8: Modal shapes for layout (a)

Figure 9: Modal shapes for layout (b)

Figure 10: Modal shapes for layout (c)

Layout	Sense spur. eigenfreq. [Hz]			Drive eigenfreq. [Hz]			Sense eigenfreq. [Hz]			First spur. eigenfreq. [Hz]		
	ROM	FEVP	Err.	ROM	FEVP	Err.	ROM	FEVP	Err.	ROM	FEVP	Err.
(a)	12356	12316	0.32%	15202	15202	0.00%	15996	15948	0.30%	18397	18397	0.00%
(b)	16318	16215	0.64%	22797	22796	0.00%	23994	23803	0.80%	27597	27596	0.00%
(c)	19201	19027	0.92%	30397	30395	0.00%	31993	31642	1.11%	36795	36792	0.00%
(d)	22646	22384	1.17%	38001	37998	0.00%	39990	38214	1.98%	45990	45986	0.00%

Table 3

Comparison between the natural frequencies computed with the ROM and the ones obtained with the full eigenvalue problem (FEVP) for the tuning fork resonator optimized layouts in Figure 12.

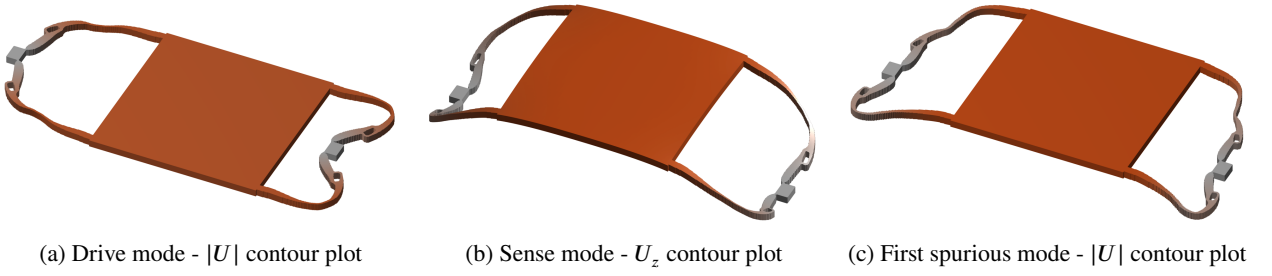


Figure 11: Modal shapes for layout (d)

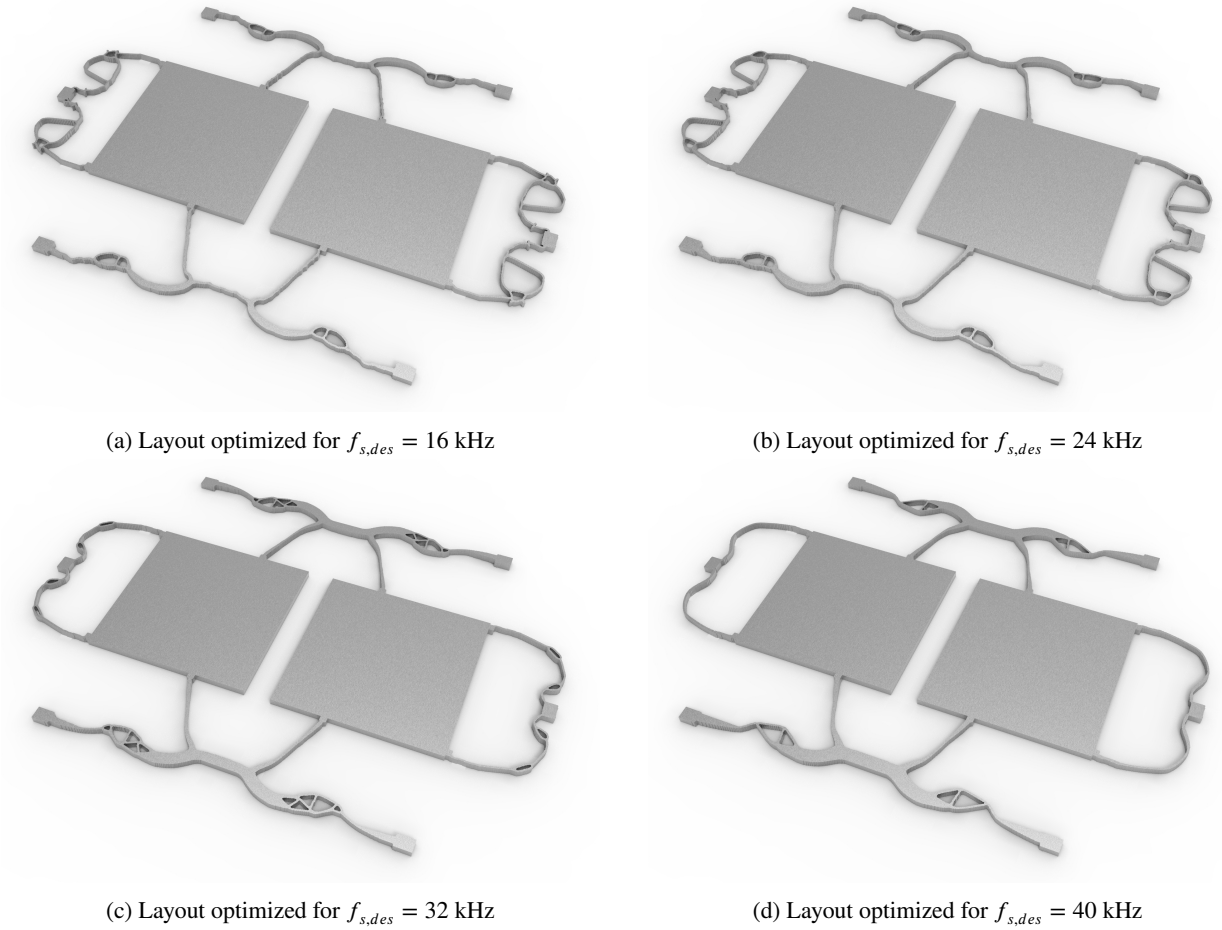


Figure 12: Tuning fork MEMS resonator design case: optimized layouts.

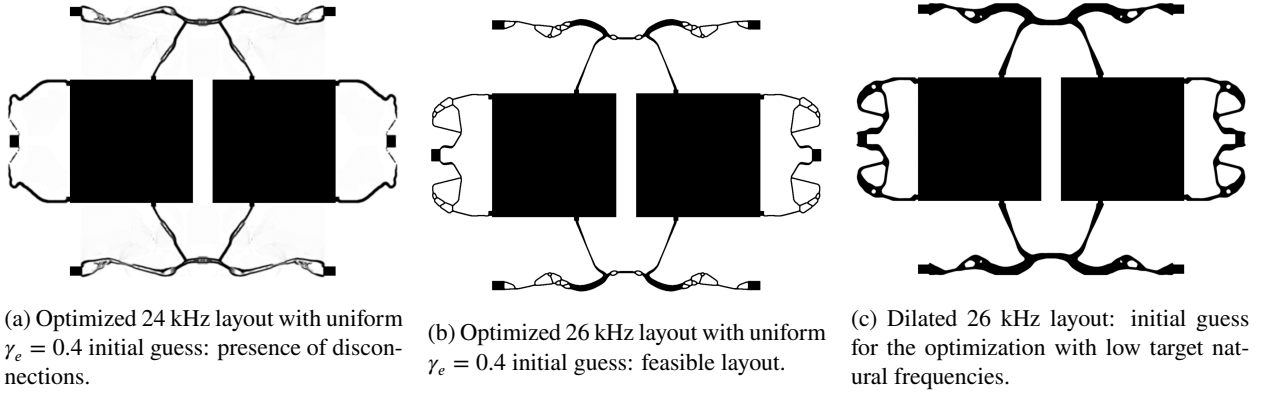


Figure 13: Tuning fork MEMS resonator design: selection of an appropriate initial guess for low frequency optimization.

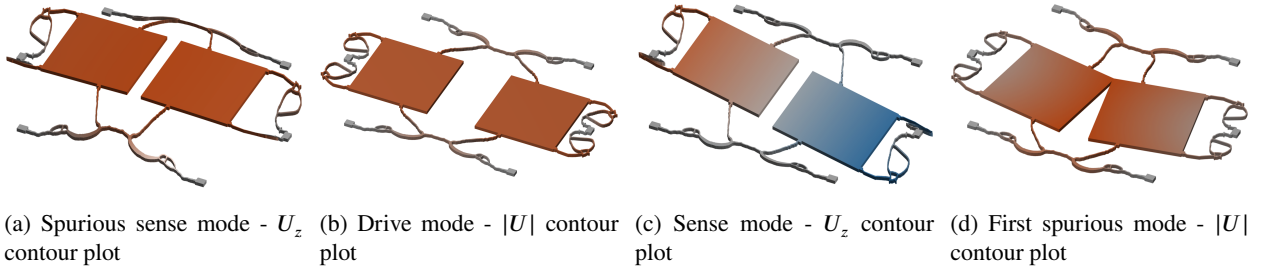


Figure 14: Modal shapes for layout (a)

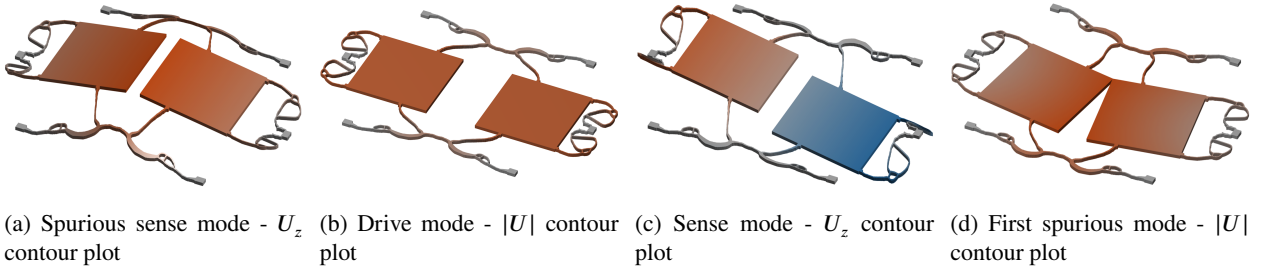


Figure 15: Modal shapes for layout (b)

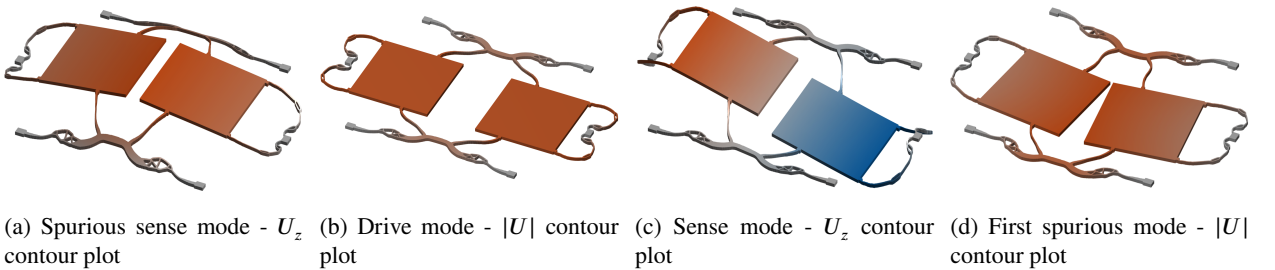


Figure 16: Modal shapes for layout (c)

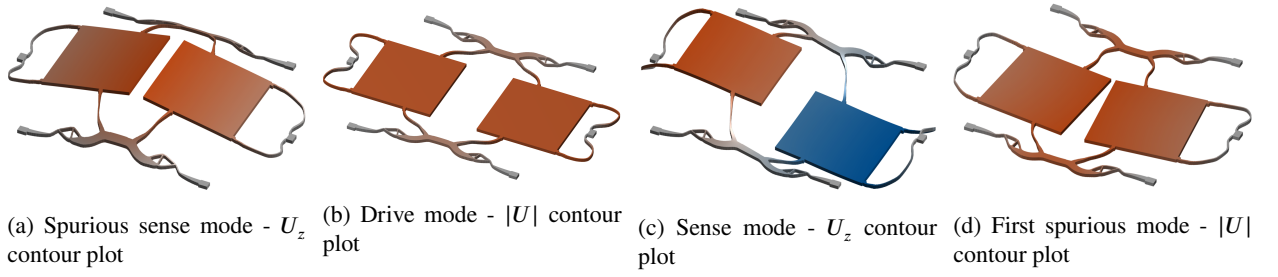


Figure 17: Modal shapes for layout (d)

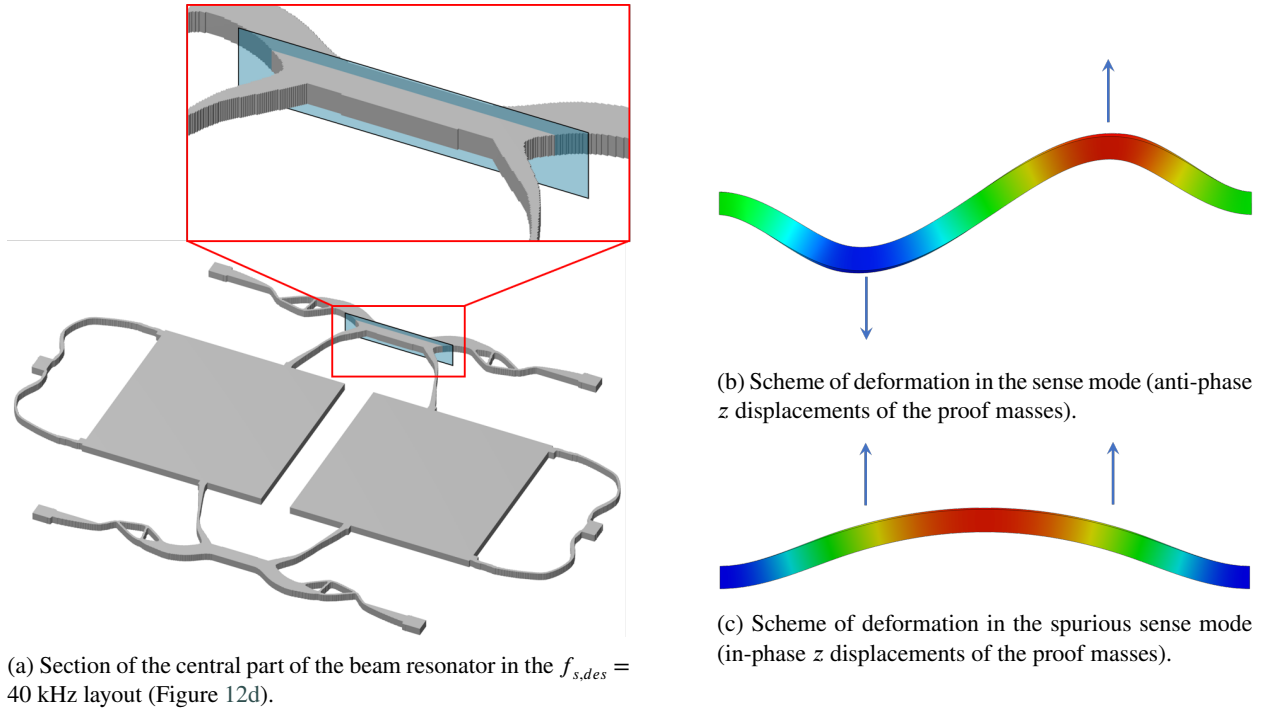


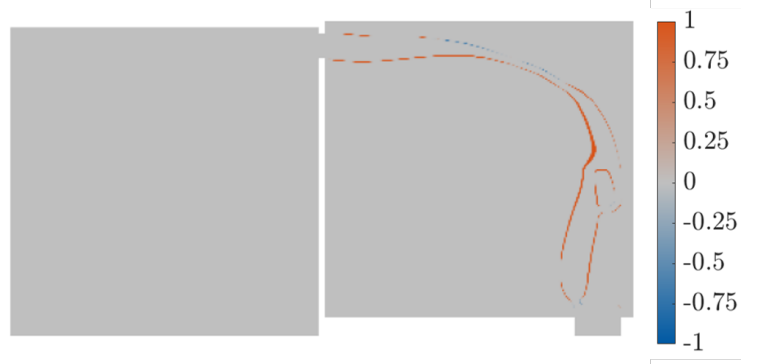
Figure 18: Central part of the additional beam resonator in the tuning fork layouts (Figure 12), and schemes of its deformation inside a section parallel to the x - z plane.



(a) Output of the optimization before fine tuning.



(b) Output of the optimization after fine tuning.



(c) Modifications of the structural layout introduced by the fine tuning procedure.

Figure 19: Analysis of the fine tuning procedure applied to the 40 kHz single mass layout (one quarter of the structure).

5. Summary and conclusions

In this paper we have presented a density based topology optimization approach to the design of MEMS resonators. The procedure generally addresses resonator layouts employing suspended proof masses or plates, where the main goal is to control the eigenfrequencies associated with specific low order modes of the structure. In particular, we have chosen MEMS gyroscopes as a suitable and industrially relevant example application, where target drive and sense natural frequencies have to be matched, and the remaining spurious modes have to be kept sufficiently far from the operation frequency range.

With onset in the working principle of MEMS gyroscopes and the associated design requirements on their natural frequencies, we have presented two model problems related to single mass and tuning fork MEMS resonators. The dynamics of the structures to be optimized have been studied through four-noded linear Mindlin shell finite elements, and reduced order models have been used to achieve numerical efficiency through the combination of multipoint constraints, static approximations and static reductions.

The topology optimization approach has been focused on the design of the connecting springs, while the resonator proof masses and anchors have been kept fixed. In the formulation of the optimization problems, geometric constraints have been used to ensure manufacturability by imposing a minimum length scale to the optimized geometric features, while explicit grey penalization constraints have been applied to address convergence to black and white layouts.

The single mass and the tuning fork resonators have been optimized for industrially acceptable target sense frequencies $f_{s,des} = 16$ kHz, 24 kHz, 32 kHz, 40 kHz. For what concerns single mass resonator, feasible layouts are achieved by simply starting the optimization procedure from a uniform density distribution. When increasing the target natural frequencies, a decreasing meandering and an increasing thickness are exploited in the connecting spring to achieve a lower overall compliance. In the tuning fork layouts case, a uniform initial guess allows to achieve feasible layouts for $f_{s,des} = 32$ kHz, 40 kHz, while we have proposed to use a dilation of the $f_{s,des} = 26$ kHz layout as initial guess to improve convergence for lower frequencies, i.e. $f_{s,des} = 16$ kHz, 24 kHz. In all the presented tuning fork resonator designs, the optimizer places an additional beam-like resonator in the coupling spring, in order to selectively increase the compliance of the spurious sense mode and keep it at a sufficiently low frequency.

The performance of the optimized layouts has been validated through a comparison with full model simulations. This shows that the chosen strategy to employ reduced order models in the optimization process, allows for well-performing resonators that are within a few percent of the target frequency in the out-of-plane direction when simulated via full models. If the final application requires a better match of the out of plane target natural frequencies, a straightforward strategy to fine tune the design is to simply continue the optimization for 50 further steps, employing only in this final phase full models for the out of plane dynamics.

Finally, the presented work will open the way for the optimization of different resonating structures in the MEMS domain, such as accelerometers, microphones, micromirrors and curved shell resonators. Possible extensions of the method can account for mechanical nonlinearities and coupled physics, including electro-mechanical and acoustic-mechanical interactions.

Acknowledgements

Daniele Giannini and Francesco Braghin acknowledge the financial support of STMicroelectronics (grant code 081/16CR). They also thank the AMG R&D team of STMicroelectronics, who provided the industrial insight and expertise that greatly assisted the research. Daniele Giannini acknowledges the partial financial support received in the framework of the ERC Starting Grant 714591 VirBAcus. Niels Aage acknowledges the support of the Villum Foundation as part of the InnoTop project.

CRedit authorship contribution statement

Daniele Giannini: conceptualization, methodology, software, formal analysis, investigation, data curation, writing (original draft), writing (review & editing), visualization. **Niels Aage:** conceptualization, methodology, software, formal analysis, investigation, data curation, writing (original draft), writing (review & editing), visualization, supervision. **Francesco Braghin:** conceptualization, methodology, resources, supervision, project administration, funding acquisition.

A. Formulation of multipoint constraints (MPC) and static reduction

Multipoint constraints (MPC) are imposed as explicit kinematic constraints between the degrees of freedom of the constrained nodes, i.e. the slave nodes s , and the centers of the proof masses, i.e. the master nodes m , namely:

$$\begin{Bmatrix} u_{x,s} \\ u_{y,s} \\ u_{z,s} \end{Bmatrix} = \begin{bmatrix} 1 & 0 & 0 & 0 & \Delta z & -\Delta y \\ 0 & 1 & 0 & -\Delta z & 0 & \Delta x \\ 0 & 0 & 1 & \Delta y & -\Delta x & 0 \end{bmatrix} \begin{Bmatrix} u_{x,m} \\ u_{y,m} \\ u_{z,m} \\ \theta_{x,m} \\ \theta_{y,m} \\ \theta_{z,m} \end{Bmatrix} \quad (22)$$

where $\mathbf{u}_m = \{u_{x,m}, u_{y,m}, u_{z,m}, \theta_{x,m}, \theta_{y,m}, \theta_{z,m}\}^T$ is the vector of degrees of freedom of the master node, $\mathbf{u}_s = \{u_{x,s}, u_{y,s}, u_{z,s}\}^T$ is the vector of translational degrees of freedom of the slave node, and $\Delta x, \Delta y, \Delta z$ are the three components of the vector connecting the master node to the slave node. We note that the rotational degrees of freedom $\theta_{x,s}, \theta_{y,s}$ of the slave node are not included in the formulation of the MPC constraints, as numerical experiments have shown that this would make the model too rigid way in the out-of-plane motion. The MPC constraints are imposed for all the nodes of the coarse structured mesh, i.e. a square region with side equal to half the side of the proof mass (cf. Figure 3): this choice has proven to be a good trade off to avoid artificial localized effects while preserving the overall compliance of the structure. The MPC equations can be then assembled together with identity equations associated with the preserved nodes (i.e. master nodes and unconstrained nodes), in order to define the transformation matrix \mathbf{T}_m employed in Eq. (3).

In order to formulate the static reduction (or Guyan reduction [56]), we first partition the vector \mathbf{u}_r into the set \mathbf{u}_r of degrees of freedom of the reduction points and the set \mathbf{u}_i of internal degrees of freedom that will be condensed out by the reduction. The reduction matrix \mathbf{T}_r is then built by the statically deformed shapes associated with independently imposed unitary displacements of the centers of the proof masses, when proper boundary conditions for the fixed anchor points are considered:

$$\mathbf{u}_m = \begin{Bmatrix} \mathbf{u}_r \\ \mathbf{u}_i \end{Bmatrix} = \mathbf{T}_r \mathbf{u}_r = \begin{bmatrix} \mathbf{I} \\ -\mathbf{K}_{m,ii}^{-1} \mathbf{K}_{m,ir} \end{bmatrix} \mathbf{u}_r \quad (23)$$

B. Sensitivity analysis

The sensitivities of natural frequencies computed from an eigenvalue problem, as used in the design of the tuning fork resonator (Eq. (20)), and the sensitivities of static estimations of natural frequencies, as used in the design of the single mass resonator (Eq. (19)), are taken from [41]. Also, the sensitivities of the spring stiffnesses k_{ij} , as introduced in the grey penalization constraints (Eq. (17)), have the same expression as the structural compliance introduced in [57]. The main difference introduced in the present work is that the system matrices have been further processed to consider multipoint constraints and static reduction (Eqs. (3) and (6)).

Since the transformation matrix \mathbf{T}_m (Eq. (3)) depends only on the nodal coordinates and keeps constant for variations in the design variables, the sensitivities of the system matrices after application of multipoint constraints can be simply written as:

$$\frac{\partial \mathbf{K}_m}{\partial \tilde{\gamma}_e} = \mathbf{T}_m^T \frac{\partial \mathbf{K}}{\partial \tilde{\gamma}_e} \mathbf{T}_m \quad \frac{\partial \mathbf{M}_m}{\partial \tilde{\gamma}_e} = \mathbf{T}_m^T \frac{\partial \mathbf{M}}{\partial \tilde{\gamma}_e} \mathbf{T}_m \quad (24)$$

The sensitivities of the reduced mass and stiffness matrices, after application of the static reduction, are:

$$\frac{\partial \mathbf{M}_r}{\partial \tilde{\gamma}_e} = \mathbf{T}_r^T \frac{\partial \mathbf{M}_m}{\partial \tilde{\gamma}_e} \mathbf{T}_r + 2\mathbf{T}_r^T \mathbf{M}_m \frac{\partial \mathbf{T}_r}{\partial \tilde{\gamma}_e} \quad \frac{\partial \mathbf{K}_r}{\partial \tilde{\gamma}_e} = \mathbf{T}_r^T \frac{\partial \mathbf{K}_m}{\partial \tilde{\gamma}_e} \mathbf{T}_r + 2\mathbf{T}_r^T \mathbf{K}_m \frac{\partial \mathbf{T}_r}{\partial \tilde{\gamma}_e} \quad (25)$$

where the sensitivities of the reduction matrix T_r (Eq. (23)) are:

$$\frac{\partial T_r}{\partial \tilde{\gamma}_e} = \begin{bmatrix} \mathbf{0} \\ \frac{\partial(-K_{m,ii}^{-1}K_{m,ir})}{\partial \tilde{\gamma}_e} \end{bmatrix} = \begin{bmatrix} \mathbf{0} \\ -K_{m,ii}^{-1} \left(-\frac{\partial K_{m,ii}}{\partial \tilde{\gamma}_e} (K_{m,ii}^{-1}K_{m,ir}) + \frac{\partial K_{m,ir}}{\partial \tilde{\gamma}_e} \right) \end{bmatrix} \quad (26)$$

The evaluation of Eq. (26) is associated with a high computational cost, since it requires one matrix multiplication and one matrix inversion per design variable. However, the possibility to neglect the the computation of the sensitivity of the reduction basis $\frac{\partial T_r}{\partial \tilde{\gamma}_e}$ (Eq. (26)) is discussed in [58, 25]. Thus, the reduced matrices sensitivities have been calculated considering only the first addends of Eq. (25).

References

- [1] C. T. . Nguyen, L. P. B. Katehi, G. M. Rebeiz, Micromachined devices for wireless communications, *Proceedings of the IEEE* 86 (8) (1998) 1756–1768. doi:10.1109/5.704281.
- [2] L. Colombo, A. Kochhar, G. Vidal-Álvarez, G. Piazza, X-cut lithium niobate laterally vibrating mems resonator with figure of merit of 1560, *Journal of Microelectromechanical Systems* 27 (4) (2018) 602–604. doi:10.1109/JMEMS.2018.2847310.
- [3] A. Kochhar, A. Mahmoud, Y. Shen, N. Turumella, G. Piazza, X-cut lithium niobate-based shear horizontal resonators for radio frequency applications, *Journal of Microelectromechanical Systems* 29 (6) (2020) 1464–1472. doi:10.1109/JMEMS.2020.3026167.
- [4] A. Partridge, H. Lee, P. Hagelin, V. Menon, We know that mems is replacing quartz. but why? and why now?, in: 2013 Joint European Frequency and Time Forum International Frequency Control Symposium (EFTF/IFC), 2013, pp. 411–416. doi:10.1109/EFTF-IFC.2013.6702311.
- [5] G. Mussi, M. Bestetti, V. Zega, A. Frangi, G. Gattere, G. Langfelder, Resonators for real-time clocks based on epitaxial polysilicon process: A feasibility study on system-level compensation of temperature drifts, in: 2018 IEEE Micro Electro Mechanical Systems (MEMS), 2018, pp. 711–714. doi:10.1109/MEMSYS.2018.8346654.
- [6] G. Mussi, M. Carrara, G. Langfelder, G. Gattere, Polysilicon mems resonator for 28-mhz oscillators, in: 2019 Joint Conference of the IEEE International Frequency Control Symposium and European Frequency and Time Forum (EFTF/IFC), 2019, pp. 1–3. doi:10.1109/FCS.2019.8856011.
- [7] C. Acar, A. Shkel, *MEMS Vibratory Gyroscopes*, MEMS Reference Shelf, Springer US, Boston, MA, 2009. doi:10.1007/978-0-387-09536-3.
- [8] V. Kempe, *Inertial MEMS*, Cambridge University Press, Cambridge, 2011. doi:10.1017/CBO9780511933899.
- [9] K. Larkin, M. Ghommam, M. Serrano, A. Abdelkefi, A review on vibrating beam-based micro/nano-gyroscopes, *Microsyst. Technol.* 0123456789 (jan 2021). doi:10.1007/s00542-020-05191-z. URL <https://doi.org/10.1007/s00542-020-05191-zhttp://link.springer.com/10.1007/s00542-020-05191-z>
- [10] A. Frangi, A. Guerrieri, R. Carminati, G. Mendicino, Parametric resonance in electrostatically actuated micromirrors, *IEEE Transactions on Industrial Electronics* 64 (2) (2017) 1544–1551. doi:10.1109/TIE.2016.2615274.
- [11] D. Brunner, H. W. Yoo, G. Schitter, Linear modeling and control of comb-actuated resonant mems mirror with nonlinear dynamics, *IEEE Transactions on Industrial Electronics* 68 (4) (2021) 3315–3323. doi:10.1109/TIE.2020.2982124.
- [12] V. R. Challa, M. G. Prasad, Y. Shi, F. T. Fisher, A vibration energy harvesting device with bidirectional resonance frequency tunability, *Smart Materials and Structures* 17 (1) (2008) 015035. doi:10.1088/0964-1726/17/01/015035. URL <https://doi.org/10.1088/0964-1726/17/01/015035>
- [13] J. Iannacci, G. Sordo, E. Serra, U. Schmid, A novel mems-based piezoelectric multi-modal vibration energy harvester concept to power autonomous remote sensing nodes for internet of things (iot) applications, in: 2015 IEEE SENSORS, 2015, pp. 1–4. doi:10.1109/ICSENS.2015.7370550.
- [14] J. Lu, T. Sagawa, L. Zhang, H. Takagi, D. F. Wang, T. Itoh, R. Maeda, Piezoelectric mems devices and its application as bio-chemical sensors, in: The 8th Annual IEEE International Conference on Nano/Micro Engineered and Molecular Systems, 2013, pp. 163–166. doi:10.1109/NEMS.2013.6559705.
- [15] S. A. Schwartz, O. Brand, L. A. Beardslee, Micromachined mass-sensitive and capacitive chemical multisensor using single polymeric sensing film, in: 2020 IEEE 33rd International Conference on Micro Electro Mechanical Systems (MEMS), 2020, pp. 721–724. doi:10.1109/MEMS46641.2020.9056216.
- [16] A. Fort, C. Trigona, E. Panzardi, V. Vignoli, T. Addabbo, M. Mugnaini, An aln micromachined mass sensor: Modeling and characterization, *IEEE Transactions on Instrumentation and Measurement* 70 (2021) 1–13. doi:10.1109/TIM.2020.3008987.
- [17] F. Laerme, A. Schilp, K. Funk, M. Offenberger, Bosch deep silicon etching: improving uniformity and etch rate for advanced mems applications, in: Technical Digest. IEEE International MEMS 99 Conference. Twelfth IEEE International Conference on Micro Electro Mechanical Systems (Cat. No.99CH36291), 1999, pp. 211–216. doi:10.1109/MEMSYS.1999.746812.
- [18] E. Benkhelifa, M. Farnsworth, A. Tiwari, G. Bandi, M. Zhu, Design and optimisation of microelectromechanical systems: a review of the state-of-the-art, *International Journal of Design Engineering* 3 (1) (2010) 41. doi:10.1504/IJDE.2010.032822.
- [19] M. Farnsworth, A. Tiwari, M. Zhu, Multi-level and multi-objective design optimisation of a MEMS bandpass filter, *Applied Soft Computing Journal* 52 (March) (2017) 642–656. doi:10.1016/j.asoc.2016.10.007.
- [20] D. Hoffmann, T. Bechtold, D. Hohlfeld, Design optimization of mems piezoelectric energy harvester, in: 2016 17th International Conference on Thermal, Mechanical and Multi-Physics Simulation and Experiments in Microelectronics and Microsystems (EuroSimE), 2016, pp. 1–6. doi:10.1109/EuroSimE.2016.7463403.

- [21] L. Li, P. Polunin, S. Dou, O. Shoshani, B. Strachan, J. Jensen, S. Shaw, K. Foster, Tailoring the nonlinear response of mems resonators using shape optimization, *Applied Physics Letters* 110 (2017) 081902. doi:10.1063/1.4976749.
- [22] V. Zega, A. Guercilena, G. Gattere, Analysis of frequency stability and thermoelastic effects for slotted tuning fork mems resonators, *Sensors* 18 (2018) 2157. doi:10.3390/s18072157.
- [23] D. Xia, L. Kong, H. Gao, A mode matched triaxial vibratory wheel gyroscope with fully decoupled structure, *Sensors (Switzerland)* 15 (11) (2015) 28979–29002. doi:10.3390/s151128979.
- [24] D. Xia, L. Kong, H. Gao, Design and analysis of a novel fully decoupled tri-axis linear vibratory gyroscope with matched modes, *Sensors (Switzerland)* 15 (7) (2015) 16929–16955. doi:10.3390/s150716929.
- [25] D. Giannini, G. Bonaccorsi, F. Braghin, Size optimization of mems gyroscopes using substructuring, *European Journal of Mechanics - A/Solids* 84 (2020) 104045. doi:https://doi.org/10.1016/j.euromechsol.2020.104045.
URL <http://www.sciencedirect.com/science/article/pii/S0997753820304332>
- [26] M. P. Bendsøe, O. Sigmund, Material interpolation schemes in topology optimization, *Archive of Applied Mechanics (Ingenieur Archiv)* 69 (9-10) (1999) 635–654. doi:10.1007/s004190050248.
- [27] N. Olhoff, Multicriterion structural optimization via bound formulation and mathematical programming, *Struct. Optim.* 1 (1) (1989) 11–17. doi:10.1007/BF01743805.
URL <http://link.springer.com/10.1007/BF01743805>
- [28] A. R. Diaaz, N. Kikuchi, Solutions to shape and topology eigenvalue optimization problems using a homogenization method, *Int. J. Numer. Methods Eng.* 35 (7) (1992) 1487–1502. doi:10.1002/nme.1620350707.
URL <http://doi.wiley.com/10.1002/nme.1620350707>
- [29] L. H. Tenek, I. Hagiwara, Static and vibrational shape and topology optimization using homogenization and mathematical programming, *Comput. Methods Appl. Mech. Eng.* 109 (1-2) (1993) 143–154. doi:10.1016/0045-7825(93)90229-Q.
URL <https://linkinghub.elsevier.com/retrieve/pii/004578259390229Q>
- [30] Z.-D. Ma, N. Kikuchi, H.-C. Cheng, Topological design for vibrating structures, *Comput. Methods Appl. Mech. Eng.* 121 (1-4) (1995) 259–280. doi:10.1016/0045-7825(94)00714-X.
URL <http://linkinghub.elsevier.com/retrieve/pii/004578259400714X><https://linkinghub.elsevier.com/retrieve/pii/004578259400714X>
- [31] X. Wang, P. Zhang, S. Ludwick, E. Belski, A. C. To, Natural frequency optimization of 3d printed variable-density honeycomb structure via a homogenization-based approach, *Additive Manufacturing* 20 (2018) 189–198. doi:https://doi.org/10.1016/j.addma.2017.10.001.
URL <https://www.sciencedirect.com/science/article/pii/S2214860417304426>
- [32] Y. Zhang, L. Gao, M. Xiao, Maximizing natural frequencies of inhomogeneous cellular structures by kriging-assisted multiscale topology optimization, *Computers & Structures* 230 (2020) 106197. doi:https://doi.org/10.1016/j.compstruc.2019.106197.
URL <https://www.sciencedirect.com/science/article/pii/S0045794919315299>
- [33] C. Jog, Topology design of structures subjected to periodic loading, *J. Sound Vib.* 253 (3) (2002) 687–709. doi:10.1006/jsvi.2001.4075.
URL <https://linkinghub.elsevier.com/retrieve/pii/S0022460X01940751>
- [34] D. Tcherniak, Topology optimization of resonating structures using SIMP method, *Int. J. Numer. Methods Eng.* 54 (11) (2002) 1605–1622. doi:10.1002/nme.484.
- [35] Z.-D. Ma, H.-C. Cheng, N. Kikuchi, Structural design for obtaining desired eigenfrequencies by using the topology and shape optimization method, *Comput. Syst. Eng.* 5 (1) (1994) 77–89. doi:10.1016/0956-0521(94)90039-6.
URL <https://linkinghub.elsevier.com/retrieve/pii/0956052194900396>
- [36] W. He, D. Bindel, S. Govindjee, Topology optimization in micromechanical resonator design, *Optimization and Engineering - OPTIM ENG* 13 (2012) 1–22. doi:10.1007/s11081-011-9139-1.
- [37] D. D. Gerrard, Y. Chen, S. A. Chandorkar, G. Yu, J. Rodriguez, I. B. Flader, D. D. Shin, C. D. Meinhart, O. Sigmund, T. W. Kenny, Topology optimization for reduction of thermo-elastic dissipation in mems resonators, in: *2017 19th International Conference on Solid-State Sensors, Actuators and Microsystems (TRANSDUCERS)*, 2017, pp. 794–797. doi:10.1109/TRANSDUCERS.2017.7994168.
- [38] F. Wein, M. Kaltenbacher, M. Stingl, Topology optimization of a cantilevered piezoelectric energy harvester using stress norm constraints, *Structural and Multidisciplinary Optimization* 48 (07 2013). doi:10.1007/s00158-013-0889-6.
- [39] M. Bruggi, V. Zega, A. Corigliano, Optimization of auxetic structures for MEMS applications, *2016 17th International Conference on Thermal, Mechanical and Multi-Physics Simulation and Experiments in Microelectronics and Microsystems, EuroSimE 2016* (2016) 1–5doi:10.1109/EuroSimE.2016.7463381.
- [40] M. A. Philippine, O. Sigmund, G. M. Rebeiz, T. W. Kenny, Topology optimization of stressed capacitive RF MEMS switches, *Journal of Microelectromechanical Systems* 22 (1) (2013) 206–215. doi:10.1109/JMEMS.2012.2224640.
- [41] D. Giannini, F. Braghin, N. Aage, Topology optimization of 2d in-plane single mass mems gyroscopes, *Structural and Multidisciplinary Optimization* (06 2020). doi:10.1007/s00158-020-02595-3.
- [42] A. M. Shkel, C. Acar, C. Painter, Two types of micromachined vibratory gyroscopes, in: *SENSORS, 2005 IEEE, 2005*, pp. 6 pp.–. doi:10.1109/ICSENS.2005.1597753.
- [43] A. Sharma, F. M. Zaman, B. V. Amini, F. Ayazi, A high-q in-plane soi tuning fork gyroscope, in: *SENSORS, 2004 IEEE, 2004*, pp. 467–470 vol.1. doi:10.1109/ICSENS.2004.1426201.
- [44] R. D. Cook, D. S. Malkus, M. E. Plesha, R. J. Witt, *Concepts and Applications of Finite Element Analysis*, 4th Edition, 2001.
- [45] M. Izadi, F. Braghin, D. Giannini, D. Milani, F. Resta, M. F. Brunetto, L. G. Falorni, G. Gattere, L. Guerinoni, C. Valzasina, A comprehensive model of beams' anisotropy in mems gyroscopes, with focus on the effect of axial non-vertical etching, in: *2018 IEEE International Symposium on Inertial Sensors and Systems (INERTIAL)*, 2018, pp. 1–4. doi:10.1109/ISISS.2018.8358126.
- [46] J. Marconi, P. Tiso, F. Braghin, A nonlinear reduced order model with parametrized shape defects, *Computer Methods in Applied Mechanics and Engineering* 360 (2020) 112785. doi:https://doi.org/10.1016/j.cma.2019.112785.

URL <https://www.sciencedirect.com/science/article/pii/S0045782519306772>

- [47] J. Marconi, G. Bonaccorsi, D. Giannini, L. Falorni, F. Braghin, Exploiting nonlinearities for frequency-matched mems gyroscopes tuning, in: 2021 IEEE International Symposium on Inertial Sensors and Systems (INERTIAL), 2021, pp. 1–4. doi:10.1109/INERTIAL51137.2021.9430478.
- [48] J. Marconi, P. Tiso, D. Quadrelli, F. Braghin, A higher-order parametric nonlinear reduced-order model for imperfect structures using neumann expansion, *Nonlinear Dynamics* (2021) 1–25 doi:10.1007/s11071-021-06496-y.
- [49] F. Wang, B. S. Lazarov, O. Sigmund, On projection methods, convergence and robust formulations in topology optimization, *Structural and Multidisciplinary Optimization* 43 (6) (2011) 767–784. doi:10.1007/s00158-010-0602-y.
- [50] M. Stolpe, K. Svanberg, An alternative interpolation scheme for minimum compliance topology optimization, *Structural and Multidisciplinary Optimization* 22 (2) (2001) 116–124. doi:10.1007/s001580100129.
- [51] N. Pedersen, Maximization of eigenvalues using topology optimization, *Structural and Multidisciplinary Optimization* 20 (1) (2000) 2–11. doi:10.1007/s001580050130.
- [52] M. Zhou, B. S. Lazarov, F. Wang, O. Sigmund, Minimum length scale in topology optimization by geometric constraints, *Computer Methods in Applied Mechanics and Engineering* 293 (2015) 266–282. doi:10.1016/j.cma.2015.05.003.
- [53] K. Svanberg, The method of moving asymptotes - A new method for structural optimization (1987). arXiv:arXiv:1011.1669v3, doi:10.1002/nme.1620240207.
- [54] O. Sigmund, Morphology-based black and white filters for topology optimization, *Structural and Multidisciplinary Optimization* 33 (4-5) (2007) 401–424. doi:10.1007/s00158-006-0087-x.
- [55] A. Seyranian, E. Lund, N. Olhoff, Multiple eigenvalues in structural optimization problems, *Structural Optimization* 8 (1994) 207–227. doi:10.1007/BF01742705.
- [56] R. J. Guyan, Reduction of stiffness and mass matrices, *Aiaa Journal - AIAA J* 3 (2) (1965) 380–380. doi:10.2514/3.2874.
- [57] M. P. Bendsoe, O. Sigmund, *Topology Optimization*, Vol. 95, Springer Berlin Heidelberg, Berlin, Heidelberg, 2004. doi:10.1007/978-3-662-05086-6.
- [58] R. T. Haftka, Z. Gürdal, *Elements of Structural Optimization*, Vol. 11 of Solid Mechanics And Its Applications, Springer Netherlands, Dordrecht, 1992. doi:10.1007/978-94-011-2550-5.



Daniele Giannini received the Ph.D. in Mechanical Engineering from Politecnico di Milano in 2020, with a thesis on innovative structural optimization methods for MEMS design and quadrature reduction in MEMS gyroscopes. He is currently postdoctoral researcher at KU Leuven, working on computational design optimization of metamaterials for vibro-acoustic applications. His research interests mainly concern structural dynamics, structural optimization, vibro-acoustics, MEMS, metamaterials, mechatronics and robotics.



Niels Aage received the PhD degree in optimal design from the Technical University of Denmark, 2011. He is an associate professor in the Department of Mechanical Engineering, Technical University of Denmark. His research interests are focused on the areas of large-scale, parallel numerical methods for PDE constrained optimization with emphasis on topology, and shape optimization problems in multiphysical settings.



Francesco Braghin received the M.Sc. degree in Mechanical Engineering and the Ph.D. degree in applied mechanics both from Politecnico di Milano (Milano, Italy), in 1997 and 2001 respectively. He became a Researcher in 2001 and in 2011 an Associate Professor in the Department of Mechanical Engineering, Politecnico di Milano, where, since 2015, he is a Full Professor in applied mechanics. His research interests are related to mechatronic systems, control engineering, robotics, vehicle dynamics, structural dynamics, MEMS and metamaterials.